Modelling snowpack on ice surfaces with the ORCHIDEE land surface model: Application to the Greenland ice sheet

Sylvie Charbit[1], Christophe Dumas[1], Fabienne Maignan[1], Catherine Ottlé[1], Nina Raoult[2], Xavier Fettweis[3], and Philippe Conesa[1]

[1]Laboratoire des Sciences du Climat et de l'Environnement, LSCE/IPSL, UMR 8212 CEA-CNRS-UVSQ, Université Paris-Saclay, 91191, Gif-sur-Yvette, France.
[2]Department of Mathematics and Statistics, Faculty of Environment, Science and Economy, University of Exeter, Laver Building, North Park Road, Exeter, EX4 4QE, United Kingdom.
[3]Laboratory of Climatology, Department of Geography, SPHERES, University of Liège, Liège, Belgium.

Correspondence to: Sylvie Charbit (sylvie.charbit@lsce.ipsl.fr)

Abstract. Current climate warming is accelerating mass loss from glaciers and ice sheets. In Greenland, the rates of mass changes are now dominated by changes in surface mass balance (SMB) due to increased surface melting. To improve the future sea-level rise projections, it is therefore critical to have an accurate estimate of the SMB, which depends on the representation of the processes occurring within the snowpack. The snow scheme (ES) implemented in the land surface model ORCHIDEE has not yet been adapted to ice-covered areas. Here, we present the preliminary developments we made to apply the ES model to glaciers and ice sheets. Our analysis mainly concerns the model's ability to represent ablation-related processes. At the regional scale, our results are compared to the MAR regional atmospheric model outputs and to MODIS albedo retrievals.

Using different albedo parameterizations, we performed offline ES simulations forced by the MAR model over the 2000-2019 period. Our results reveal a strong sensitivity of the modeled SMB components to the albedo parameterization. Results inferred with albedo parameters obtained with a manual tuning approach present a very good agreement with the MAR outputs. Conversely, with the albedo parameterization used in the standard ORCHIDEE version, runoff and sublimation were underestimated. We also tested parameters found from a previous data assimilation experiment calibrating the ablation processes using MODIS snow albedo. While these parameters greatly improve the modelled albedo over the entire ice sheet, they degrade the other model outputs compared to those obtained with the manually-tuned approach. This is likely due to the model overfitting to the calibration albedo dataset without any constraint applied to the other processes controlling the state of the snowpack. This underlines the need for performing a "multi-objective" optimisation using auxiliary observations related to snowpack internal processes. Although there is still room for further improvements, the developments reported in the present study constitute an important advance in assessing the Greenland SMB with possible extension to mountain glaciers or the Antarctic ice sheet.

1. Introduction

Satellite observations reveal that the Greenland ice sheet (GrIS) has been losing mass for at least three decades. Between 1992 and 2018, the net ice mass loss was estimated at 3800 ± 339 Gt, corresponding to a rise in global mean sea level of 10.6 ± 0.9 mm (The IMBIE team, 2020). Mass loss is driven by dynamic solid ice discharges (Enderlin et al., 2014) and by enhanced surface meltwater and runoff (Ryan et al., 2019). Over the 2000-2008 period, the GrIS mass loss was equally partitioned between surface and dynamic processes (van den Broeke et al.,

2009). However, recent studies based on regional climate models and remote sensing observations (van den Broeke, 2016; Ryan et al., 2019; The IMBIE Team, 2020, Fox-Kemper et al., 2021) show that rates of mass change are now dominated by changes in surface mass balance (SMB), defined as the difference between mass gains (solid and liquid precipitation) and surface ablation processes (runoff, sublimation and snow erosion).

Besides directly impacting the global mean sea level, the GrIS is also an integral part of the Earth System (Fyke et al., 2018). As such, it is highly sensitive to climate change and in turn, has a strong influence on global climate, notably by releasing fresh water into the ocean, which leads to changes in the Atlantic meridional overturning circulation (Bakker et al., 2016; Martin et al., 2022). Surface melting may also induce changes in the local climate through the temperature-elevation feedback (Edwards et al., 2014; Sellevod et al., 2019) and the albedo effect (Box et al., 2012; Helsen et al., 2017; Riihelä et al., 2019). Finally, changes in topography produce modifications of the local and large-scale atmospheric circulations (Ridley et al., 2005; Hahn et al., 2020).

To capture this feedback and to reduce the uncertainties in sea-level and climate projections, a key objective of the climate-ice sheet modelling community is to incorporate ice-sheet models in Earth System Models (ESMs) (Vizcaino, 2014). Such coupled climate-ice sheet models have mainly been developed with low resolution climate models designed for long-term integrations (Kageyama et al., 2004; Charbit et al., 2005; Vizcaino et al., 2010; Roche et al., 2014). So far, only a few groups have met this goal with CMIP-like models (Vizcaino et al., 2013; Muntjewerf et al., 2020; Smith et al., 2021). A key challenge in developing such models relates to the realistic computation of SMB used as a forcing field of the ice-sheet models.

SMB is highly dependent on the radiative properties of snow and on the physical processes occurring within the snowpack (Helsen et al., 2017). At the surface, snow cover evolves as a function of the surface energy balance and mass exchanges with the atmosphere. In cold regions, snow melt is largely driven by shortwave radiation: Because of the high albedo value of fresh snow (0.80 – 0.90), a large fraction of shortwave radiation is reflected to the atmosphere, limiting the energy available at the surface for melting. Therefore, snow evolution is strongly dependent on the albedo. The value of snow albedo decreases when snow is ageing (i.e. in the absence of a new snowfall event) and with the snow metamorphism and liquid water content at the ice sheet's surface coming either from rainfall or from snow/ice melting. Surface water may also percolate and refreeze inside the snowpack, thereby delaying the runoff. The transformation of snow into ice depends on environmental conditions (e.g. winds, near-surface temperatures) and internal processes within the snowpack (e.g. heat conduction and vertical temperature gradient, compaction), which directly influence the grain microstructure and the snow density. All these processes affect the SMB of the ice sheet.

There are several ways to compute the SMB. Empirical approaches such as the positive degree-day method (Reeh, 1991) have long been used to compute snow and ice melting from downscaled near-surface temperatures. This kind of approach requires little computational resources and has often been applied for past and future long-term integrations (Charbit et al., 2008; 2013; Bonelli et al., 2009; Vizcaino et al., 2010). However, such methods have been calibrated against the present state of the GrIS, raising the question as to whether they can be applied in a different climatic context from the present-day one knowing that ablation is projected to increase (van de Wal, 1996; Bougamont et al., 2007). Moreover, they are not physically-based and cannot reproduce the diversity of snow processes that directly influence the SMB. Snow models implemented in general circulation models have long been based on simplified physics. They are mainly designed to resolve the seasonal and diurnal variations of heat fluxes, but with no representation of internal processes (Armstrong and Brun, 2008). By contrast, regional

78   climate models developed for polar regions generally incorporate multiple-layer energy balance snow models with

79   a fine vertical resolution (e.g. Brun et al., 1992; Lefebre et al., 2003; Vionnet et al., 2012; Noël et al., 2018) and

80   with detailed snow physics to simulate a variety of snowpack processes. However, due to their high computational

81   cost, they are not often used in ESMs, despite a few rare exceptions such as the work of Punge et al. (2012) based

82   on the implementation of a detailed snow model (Brun et al., 1992) in the atmospheric model LMDZ4 (Hourdin

83   et al., 2006), or the Community Land Model (CLM) which includes the snow radiative transfer scheme SNICAR

84   (Flanner and Zender, 2006) and a snow model simulating a variety of key snow processes such as the

85   metamorphism (Lawrence et al., 2019, He et al., 2024).

86   An alternative approach consists in implementing snow models of intermediate complexity in the land surface

87   components of ESMs (Boone and Etchevers, 2001; Dutra et al., 2010; Wang et al., 2013; Cullather et al., 2014;

88   Decharme et al., 2016; Born et al., 2019). These models have a limited number of layers and are based on simplified

89   representations of the main processes affecting the SMB changes, but usually do not have any explicit

90   representation of snow metamorphism. However, they offer a good compromise between models of high

91   complexity and simplified approaches or bulk-layer models for coupling with atmospheric models.

92   The snow module Explicit Snow (referred hereafter to as ES) implemented in the land surface model ORCHIDEE

93   (Organising Carbon and Hydrology In Dynamic Ecosystems; Krinner et al., 2005; Chéruy et al., 2020) of the

94   IPSL-CM ESM (Boucher et al., 2020) belongs to this third class of snow models. It has been successfully evaluated

95   against observations in Col de Porte (French Alps) and in various sites of Northern Eurasia (Wang et al., 2013).

96   However, it has not yet been adapted to ice-covered areas. As a result, glaciers are considered as bare soils in the

97   current ORCHIDEE version, and over ice sheets, snow is handled with the atmospheric component of IPSL-CM

98   in a very simplistic way. Recently, we made new developments to apply the ES model to glaciers and ice sheets,

99   with a special focus on the GrIS. These developments meet two objectives. The first one is to treat snow-related

100   processes in IPSL-CM in a more consistent way for all surface types. The second one is to compute the SMB,

101   taking the main processes occurring within the snowpack into account. These developments also constitute a

102   preliminary step for the subsequent use of the computed SMB as an interface between IPSL-CM and ice-sheet

103   models. In the following, we will refer to ORCHIDEE-ICE to deal with the version of ORCHIDEE that includes

104   these new developments, and to ORCHIDEE to deal with the former version of the model.

105   In this study, we evaluate the computation of SMB (and its components) in the ES model. As SMB is strongly

106   dependent on the albedo, we also examine its sensitivity to various albedo parameterizations. To achieve this, we

107   performed offline ORCHIDEE-ICE simulations and compared our results against model outputs from the polar-

108   oriented regional atmospheric model MARv3.11.4 (Modèle Atmosphérique Régional, Fettweis et al., 2017) and

109   the MODIS (MODerate resolution Imaging Spectroradiometer, Hall et al., 1995; Hall and Riggs, 2016) surface

110   albedo retrievals. The paper is organized as follows. In Section 2, we provide an extensive description of the main

111   characteristics of the original ES model as well as changes that occurred since its early publication (Wang et al.,

112   2013). The new developments made for applying ES to the GrIS are also presented in this section. Section 3

113   describes the experimental setup and Section 4 provides a brief overview of the different datasets used for

114   evaluation. The results are presented in Sections 5 and 6 and discussed in Section 7.

115

2. Model description

2.1 Snow processes in the current ORCHIDEE-AR6 model

ORCHIDEE is the land surface component of the IPSL-CM Earth System Model (Boucher et al., 2020; Chéruy et al., 2020) mainly developed at the French Institute Pierre Simon Laplace (IPSL). It computes both the water and energy exchanges (SECHIBA module) between land surfaces and the atmosphere at a half-hourly time step and includes carbon-related processes (STOMATE module). Within a given grid cell, land cover is represented as fractions of bare soils and vegetated areas described in terms of plant functional types (PFTs). The snow-vegetation interactions are not explicitly represented and snow is evenly distributed among the various PFTs. Soil types are prescribed according to the USDA soil texture maps (Reynolds et al., 2000). The ORCHIDEE model can be run in off-line mode, driven by atmospheric fields, or coupled with an atmospheric model. In the former ORCHIDEE version used for CMIP5 (Taylor et al., 2012), the snow scheme over glaciated surfaces was based on the bulk approach proposed by Chalita and Le Treut (1994). It consisted of a composite soil-snow model accounting for the thermal and radiative properties of snow cover (i.e. albedo and its variations with snow ageing). Snow was described as having a constant density (330 kg m^{-3}) and melting occurred when temperature exceeded 0°C. Other processes such as water percolation and refreezing were ignored, although they directly impact the water budget. This means that all liquid water coming from melting snow was leaving the snowpack as runoff.

For the CMIP6 exercise (Eyring et al., 2016), the bulk approach has been replaced by the ES snow scheme, which was formerly adapted to the ORCHIDEE architecture (Wang et al., 2013) from a three-layer version of the ISBA-ES scheme (Interactions between Soil, Biosphere and Atmosphere-Explicit Snow scheme; Boone and Etchevers, 2001) developed at the French National Center for meteorological Research. The ES model is now used in the standard version of ORCHIDEE (version 2.0 onwards). However, it has not yet been considered for use over mountainous glaciers, which are treated as bare soils, nor over ice sheet areas, which are currently handled by the LMDZ atmospheric model (Chéruy et al., 2020) with a very elementary snow scheme (i.e. single-layer model, constant albedo and thermal conductivity). In this section, we provide an extensive description of the snow model, including the main differences with the original ISBA-ES version (Wang et al., 2013). The new developments accounting for snow processes over ice-covered areas in the ORCHIDEE model are described in section 2.2.

The ES model represents the snowpack as a one-dimensional physical system (vertical coordinate z). This means that all the lateral fluxes of mass and energy are ignored. The original version of this snowpack is discretized in three layers following the parameterization of Lynch-Stieglitz (1994), which sets the upper limits for the thickness of the first two layers at 5 and 50 cm respectively. This ensures the propagation of variations in the diurnal cycle of temperature and radiation, and enables vertical heat and density gradients, which are assumed to be larger near the surface, to be resolved correctly. Each layer is described in terms of snow density, snow age, layer thickness, heat content, snow temperature and liquid water content, with the first three variables being prognostic variables. Changes in snow mass are determined by the snowfall rate, snow melting, runoff at the base of the snowpack and sublimation at the surface. In the absence of coupling with a dynamic ice sheet model, snow mass at the surface of the ice sheet can be overestimated. Thus, to prevent excessive snow accumulation, we impose a maximum threshold of 3000 kg m^{-2} beyond which snow is artificially removed. An overview of the organization of the different subroutines of the ES snowpack model is provided in Figure 1. The description of the processes is given in the following subsections and the list of model parameters is provided in Table A1 (Appendix A).
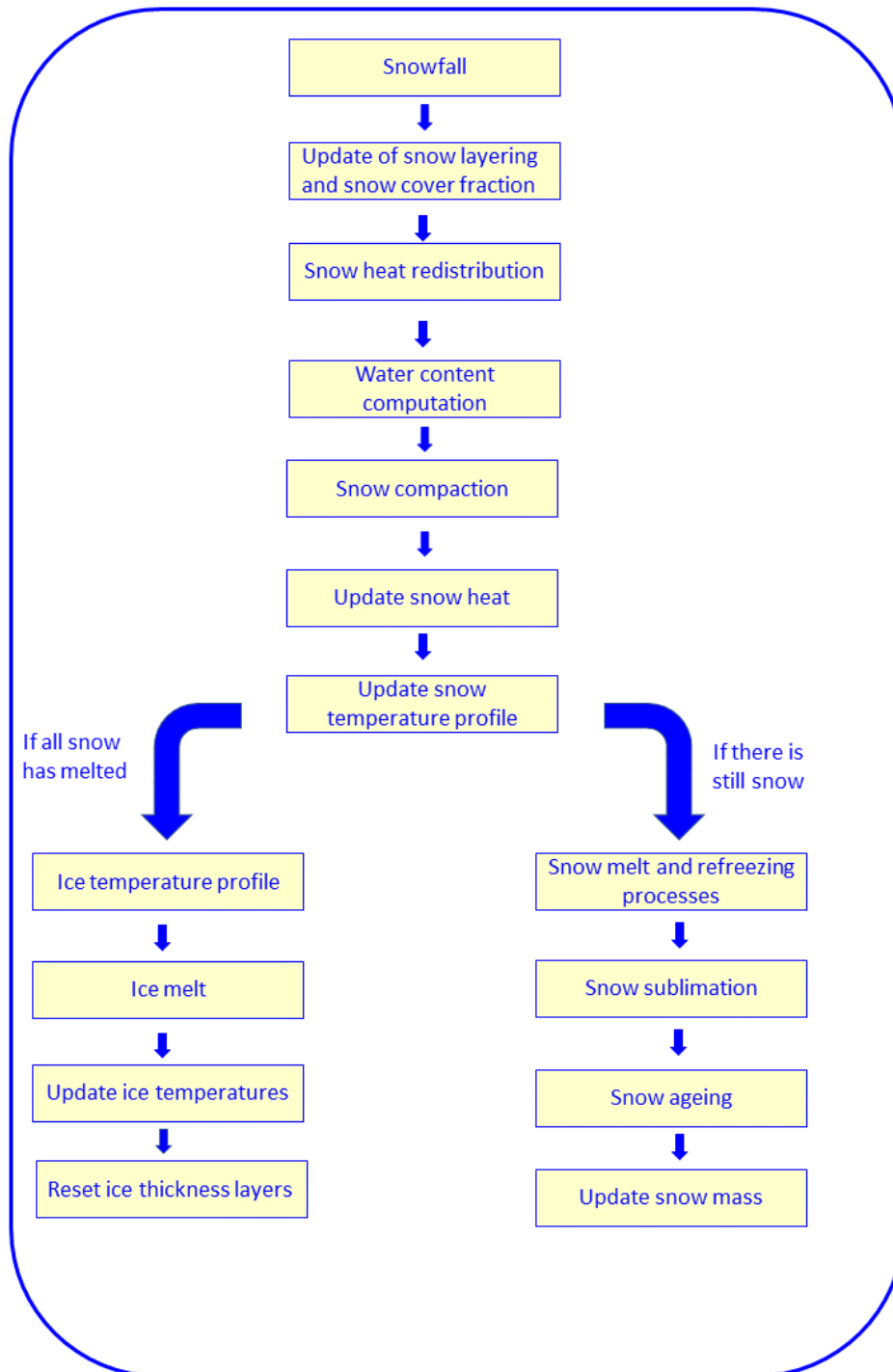
156

157   **Figure 1:** Flowchart of the new Explicit Snow scheme implemented in the ORCHIDEE-ICE model.

158

159

160

161

2.1.1 Surface processes

Energy balance

The evolution of the snowpack is primarily driven by the energy flux at the snow-atmosphere interface. A single energy balance is computed for all surface types coexisting in one grid cell. The surface energy flux (G_{surf}) available at the snow-atmosphere interface is computed from the energy balance equation:

$$G_{surf} = SW_{net} + LW_{net} - H_L - H_S + H_{rainfall} \tag{1}$$

G_{surf} is computed positively when it warms the soil. SW_{net} and LW_{net} are the net shortwave and longwave radiations respectively, H_L is the latent heat flux, H_S is the sensible heat flux and $H_{rainfall}$ is the energy released by rainfall (see Eq. (14) in Boone and Etchevers, 2001). Equation (1) is used to compute the surface temperature (T_{surf}) of the grid cell at the next time step and provides the limit condition of the surface temperature at the snow-atmosphere interface for the calculation of the snow temperature profile.

Above snow-covered surfaces, when T_{surf} is above the freezing temperature T_0 (273.15 K), the energy excess is first used to bring the snow temperature to T_0. A surface energy flux $G_{freezing}$ associated with the freezing temperature T_0 can be computed using a similar formulation to Eq. (1). The difference between G_{surf} and $G_{freezing}$ is converted in an additional temperature expressed as:

$$T_{snow}^{add} = T_{surf} - T_0 = \frac{G_{surf} - G_{freezing}}{C_{soil}} \, dt \tag{2}$$

C_{soil} is the surface heat capacity of soil (J m^{-2} K^{-1}) and is computed as the sum of heat capacities for snow-covered and snow-free surfaces (for both non-glaciated and glaciated areas) weighted by their respective grid cell fractions. For snow-covered surfaces, the specific heat capacity is defined as the product of snow density and the specific heat of ice (2106 J K^{-1} kg^{-1}). If T_{snow}^{add} is greater than (or equal to) the freezing temperature, the energy excess is used for melting snow, and G_{surf} is further set to $G_{freezing}$ for energy conservation. If the new G_{surf} value is greater than the total heat content of the snowpack, snow is entirely melted and the excess energy is transferred to the underlying soil. The energy released by snowfall is accounted for in the snowpack scheme to update the snow heat content of the snowpack after a snowfall event.

Turbulent heat fluxes

The sensible (H_S) and latent heat (H_L) fluxes computed for each grid cell are given respectively by:

$$H_S = \rho_{air} q_{cdrag} U (T_{surf} - T_{air}) \tag{3}$$

$$H_L = L_s \rho_{air} q_{cdrag} U (Q_{sat} - Q_{air}) \tag{4}$$

where ρ_{air} is the air density, T_{surf} and T_{atm} are the surface and the 2 m atmospheric temperatures, Q_{air} and Q_{sat} are the air specific humidity at 2 m and the saturated specific humidity at the surface, L_s is the latent heat of sublimation (2.8345 10^6 J kg^{-1}), U is the wind speed at 10 m and q_{cdrag} is the drag coefficient computed as a function of the ice roughness length (*z0_ice* = 0.001 m), following the Monin-Obukhov turbulence theory (Monin and Obhukov, 1954) and the parameterizations of the eddy fluxes proposed by Louis (1979).

197 *Snow sublimation*

198 The amount of sublimation is simply deduced from the latent heat flux:

199 $$S_{snow} = \frac{H_L}{L_s}$$ (5)

200 *Snow cover fraction*

201 The snow cover fraction (F_{snow}) is derived from the formulation of Niu and Yang (2007) which has been shown

202 to better represent the seasonal variation of the relationship between snow depth (Z_{snow}) and snow cover fraction

203 thanks to its dependence on snow density:

204 $$F_{snow} = \tanh\left(\frac{Z_{snow}}{2.5 z_{0g} \times \left(\frac{\langle \rho_{snow} \rangle}{\rho_{min}}\right)^m}\right)$$ (6)

205 where $\langle \rho_{snow} \rangle$ is the snow density averaged over the total thickness of the snowpack, ρ_{min} is the minimum snow

206 density (set to 50 kg m^{-3}), that is the density of fresh snow, z_{0g} is the ground roughness length (set to 0.01 m) and

207 m (set to 1.0 in the present study) is an adjustable parameter.

208 *Snow albedo*

209 Compared to the early version presented in Wang et al. (2013), the albedo scheme has been modified and snow

210 albedo is now computed following the formulation of Chalita and Le Treut (1994):

211 $$\alpha_{snow} = A_{aged} + B_{dec} \exp\left(-\frac{\tau_{snow}}{\tau_{dec}}\right)$$ (7)

212 where A_{aged} represents the albedo of a snow-covered surface after snow ageing (old snow) and B_{dec} is defined so

213 that the sum of A_{aged} and B_{dec} represents the albedo of fresh snow (i.e. maximum snow albedo). τ_{dec} is the time

214 constant of the albedo decay and τ_{snow} is the snow age and is parameterized as follows:

215 $$\tau_{snow}(t + dt) = \left[\tau_{snow}(t) + \left(1 - \frac{\tau_{snow}}{\tau_{max}}\right) \times dt\right] \times \exp\left(-\frac{P_{snow}}{\delta_c}\right) + f_{age}$$ (8)

216 where τ_{max} is the maximum snow age, P_{snow} is the amount of snowfall during the time interval dt and δ_c is the

217 critical value of solid precipitation necessary for reducing the snow age by a factor 1/e. As the ORCHIDEE time

218 step is fixed to 30 mn,, the snow age is almost zero in a few time steps. In addition, low surface air temperatures

219 found in polar regions slow down the metamorphism. This effect is accounted for with the function f_{age} expressed

220 as:

221 $$f_{age} = \left[\frac{\left(\tau_{snow}(t) + \left(1 - \frac{\tau_{snow}}{\tau_{max}}\right) \times dt\right) \times \exp\left(-\frac{P_{snow}}{\delta_c}\right) - \tau_{snow}(t)}{1 + g_{temp}(T_{surf})}\right]$$ (9)

222 $$g_{temp}(T_{surf}) = \left[\frac{max(T_0 - T_{surf},\ 0)}{\omega_1}\right]^{\omega_2}$$ (10)

223 where ω_1 and ω_2 are tuning constants. The albedo is computed for the visible and near-infrared spectral bands.

224 However, to compute the upward shortwave radiation, an arithmetic mean between the visible and the near-

225 infrared albedo is considered.

226 A single energy balance is computed for all surface types but the albedo is weighted by the different fractions of

227 PFTs and glaciated areas and by the snow-covered and snow-free fractions. As a result, the surface albedo (α) of

228   the grid cell is computed as the sum of snow-free albedo ($\alpha_{snow-free}$) and snow-covered albedo (α_{snow}) weighted

229   by the fractional area of the grid cell covered by snow F_{snow} (snow-covered fraction hereafter):

230    $$\alpha = F_{snow} \times \alpha_{snow} + (1 - F_{snow}) \times \alpha_{snow-free} \tag{11}$$

231   with:

232    $$\alpha_{snow} = f_{ice} \times \alpha_{snow}^{ice} + \sum_{PFT} f_{PFT,i} \times \alpha_{snow}^{PFT,i} \tag{11a}$$

233   and:

234    $$\alpha_{snow\_free} = f_{ice} \times \alpha_{snow\_free}^{ice} + \sum_{PFT} f_{PFT,i} \times \alpha_{snow\_free}^{PFT,i} \tag{11b}$$

235   f_{ice} and $f_{PFT,i}$ are the grid cell fractions of ice-covered areas and the ith PFT respectively; α_{snow}^{ice} (resp. $\alpha_{snow\_free}^{ice}$)

236   and $\alpha_{snow}^{PFT,i}$ (resp. $\alpha_{snow\_free}^{PFT,i}$) are the corresponding snow albedo (resp. snow-free albedo) values.

237   Over the GrIS, $\alpha_{snow-free}$ is given by the albedo of bare ice, prescribed to 0.6 and 0.2 for visible and near-infrared

238   wavelengths respectively. At the margins of the GrIS, some grid points may be only partially covered by snow or

239   ice, or even become totally snow-free during the melting season. It is therefore important to take these different

240   features into account to compute correctly the surface albedo of the GrIS.

241   **2.1.2 Internal processes**

242   When snow falls on a snow-free surface, a new snowpack is generated providing that the ground temperature is

243   below or equal to the freezing point. The snow mass and the heat content of the snowfall are initially distributed

244   evenly within the three layers. The snow density is the same for the three layers and is given by the density of the

245   snowfall computed as a function of wind speed and surface air temperature (Pahaut, 1976). When snowfall occurs

246   over an existing snowpack, fresh snow is added to the upper layer providing that the snowfall thickness is greater

247   than the critical threshold δ_c (see Eq. 8). The snow thickness, density and heat content are then modified in this

248   layer. However, as the number of snow layers is kept fixed, redistribution of mass and heat content within the

249   layers is required when snow depth changes, but the total snow mass and heat content are conserved.

250   *Heat conduction*

251   Solar absorption is not accounted for in the snow model. All incoming solar energy is therefore deposited at the

252   snow surface and distributed in deeper layers through heat conduction. The heat conduction from the surface to

253   the bottom of the snowpack is described by a vertical diffusion equation relating the temporal evolution of the

254   snow temperature in the snowpack at a depth z and the divergence of the snow heat flux F_C and is solved using an

255   implicit numerical scheme.

256    $$\frac{\partial T_{snow}}{\partial t} = -\frac{1}{C_{snow}} \cdot \frac{\partial F_C}{\partial z} \tag{12}$$

257    $$F_C = -\Lambda_s \frac{\partial T_{snow}}{\partial z} \tag{13}$$

258   with C_{snow} (J m^{-2} K^{-1}) Λ_s and T_{snow} being the snow heat capacity, the snow thermal conductivity (W m^{-1} K^{-1}) and

259   the snow temperature respectively.

260   At the snow-atmosphere interface, the boundary condition is given by the energy balance equation ($F_c = G_{surf}$)

261   and is used in the ORCHIDEE model to compute the surface temperature.

Along with the thermal gradient, a water vapor diffusive flux takes place from the warmer to the colder parts of the snowpack and sublimation or condensation may occur in the pore spaces depending on the water vapor saturation pressure. This process is particularly significant in the Arctic because of strong temperature gradients between soils and atmosphere and is in great part responsible for snow metamorphism. While it is explicitly accounted for in detailed snow models, in Explicit Snow, the effect of water vapor diffusion and phase changes is parameterized through the thermal conductivity (Sun et al., 1999). An effective thermal conductivity (Λ_{eff}) is thus expressed as the sum of empirical formulations for snow thermal conductivity (Λ_{cond}) and thermal conductivity from vapor transport (Λ_{vap}), with:

$$\Lambda_{cond}^i = a_\lambda + b_\lambda \rho_{snow}^{i}{}^2 \tag{14}$$

$$\Lambda_{vap}^i = \left(a_{\lambda v} + \frac{b_{\lambda v}}{c_{\lambda v} + T_{snow}^i}\right)\frac{P_0}{P} \tag{15}$$

With a_λ= 0.02 W m^{-1} K^{-1}, b_λ = 2.5 10^{-6} W m^5 K^{-1} kg^{-2} (Anderson, 1976), $a_{\lambda v}$ = -0.06023 Wm^{-1}K^{-1}, $b_{\lambda v}$ = -2.5425 W m^{-1} and $c_{\lambda v}$ = -289.99 K (Yen, 1981). P is the atmospheric pressure in hPa and P_0 = 1000 hPa. The superscripts i denote the ith layer.

Heat content

The heat content is computed using the following equation:

$$H_{snow}^i = D_{snow}^i\left[C_{snow}^{v,i}\left(T_{snow}^i - T_f\right) - L_s\rho_{snow}^i\right] + L_f\rho_{water}W_{liq}^i \tag{16}$$

where L_f is the latent heat of fusion and ρ_{water} is the water density. H_{snow}^i , W_{liq}^i, D_{snow}^i, ρ_{snow}^i and $C_{snow}^{v,i}$ are the heat and liquid contents, the depth, the density and the mean volumetric heat capacity (J K^{-1} m^{-3}) of the ith layer.

After heat redistribution within the snowpack, snow temperature is diagnosed using Eq. (16), assuming no liquid water in the snowpack. If snow temperature exceeds the freezing point, the liquid content in each layer is then diagnosed from the snow temperature and heat content of the layer, and the temperature is then reset to the freezing point.

Compaction

The total snow depth decreases as density increases. Changes in density occur as a result of the weight of the overlying snow layers and under the influence of snow metamorphism. The local rate of density change in the ith layer is derived from Anderson (1976):

$$\frac{1}{\rho_{snow}^i}\frac{\partial \rho_{snow}^i}{\partial t} = \frac{\sigma_{snow}^i}{\eta_{snow}^i\left(T_{snow}^i, \rho_{snow}^i\right)} + \psi_{snow}^i\left(T_{snow}^i, \rho_{snow}^i\right) \tag{17}$$

The first term of the right-hand side represents the compaction due to snow load, with σ_{snow}^i (Pa) being the pressure of the overlying snow and η_{snow}^i the snow viscosity.

$$\sigma_{snow}^i = g \ x \ M_{snow}^i$$

where g is the gravitational constant (m s^{-2}) and M_{snow}^i the cumulative snow mass (kg m^{-2}).

The viscosity (in Pa s) is expressed as a function of snow temperature and density (Mellor, 1964; Kojima, 1967):

$$\eta_{snow}^i = \eta_0 exp\left[a_\eta\left(T_f - T_{snow}^i\right) + b_\eta\rho_{snow}^i\right] \tag{18}$$

296   with $\eta_0 = 3.7 \times 10^7$ Pa s, $a_\eta = 8.1 \times 10^{-2}$ K^{-1} and $b_\eta = 1.8 \times 10^{-2}$ m^3 kg^{-1}.

297   The second term in the right-hand side of Eq. (17) parameterizes the effect of metamorphism which is significant

298   for newly fallen snow.

299    $$\psi_{snow}^i = a_\psi exp\left[- b_\psi \cdot \left(T_f - T_{snow}^i\right) - c_\psi \cdot max\left(0, \rho_{snow}^i - \rho_\psi\right)\right] \tag{19}$$

300   The values of the parameters are the following: $a_\psi = 2.8 \times 10^{-6}$ s^{-1}, $b_\psi = 4.2 \times 10^{-2}$ K^{-1}, $c_\psi = 460$ m^{3}kg^{-1}, $\rho_\psi = 150$

301   kg m^{-3}.

302   In the model, density changes due to compaction are allowed as long as density remains below a threshold fixed

303   to 750 kg m^{-3}. This value was chosen because compaction becomes slower above densities between 550 and 800

304   kg m-3 due to the progressive disappearance of air spaces between the snow particles (Maeno and Ebinuma, 1983).

305   A critical value of 730 kg m-3 has even been advanced by Maeno (1978). Compaction does not affect the total

306   mass and the heat content of the snowpack but changes the layer thicknesses. The distribution of snow heat within

307   the layers must therefore be updated using Eq. (16).

308   *Vertical temperature profile*

309   The snow temperature profile resulting from heat redistribution is then computed by solving the heat diffusion

310   equation using an implicit numerical scheme similar to that used for heat diffusion in the soil. The vertical

311   temperature profile within the snowpack is expressed as:

312   For the 1st layer:

313    $$T_{snow}^1 = \left[\frac{\lambda_{snow} \cdot C_{gr\_snow} + \left(T_{surf} + T_{snow}^{add}\right)}{1 + \lambda_{snow}\left(1 - D_{gr\_snow}\right)}\right] \tag{20}$$

314   For the deeper layers (i > 1):

315    $$T_{snow}^{i+1} = C_{gr\_snow} + D_{gr\_snow} \cdot T_{snow}^i \tag{21}$$

316   where λ_{snow}, C_{gr_snow}, D_{gr_snow} are coefficients resulting from the resolution of the numerical scheme and depend

317   on the snow heat capacity, thermal conductivity and characteristics of the vertical discretization. The numerical

318   scheme is similar to the one presented in Wang et al. (2016, see Appendix A therein) in which the temperature at

319   the interface between two layers is calculated as a linear interpolation according to the two nearest nodes (middle

320   of the layers). Diffusion therefore takes place downward and upward.

321   *Melting and refreezing processes*

322   If melt water is produced at the surface, it may remain in the liquid state in the uppermost layer or penetrate the

323   next layer where it can remain or refreeze as long as the maximum water holding capacity is not reached; otherwise,

324   it penetrates the lower layers.

325   The evolution of liquid water in each layer is controlled by the energy available to induce phase changes and by

326   the maximum water holding capacity. In the ith layer, the energy used for melting snow (E_{snow}^i) is expressed as:

327    $$E_{snow}^i = min\left(C_{snow}^{v,i} D_{snow}^i \times max\left(0, T_{snow}^i - T_f\right), max\left(0, D_{swe}^i - W_{liq}^i\right) \times L_f \rho_{water}\right) \tag{22}$$

328   where D_{swe}^i is the snow water equivalent in the ith layer. The first term represents the available energy for phase

329   change in the ith layer and the second term corresponds to the energy required to melt entirely the snow mass that

330   has not been transformed into liquid water. The maximum water holding capacity is taken from Anderson (1976):

331 $$W_{max}^i = \left[r_{min} + (r_{max} - r_{min}) \cdot max\left(0, \frac{\rho_t - \rho_{snow}^i}{\rho_t}\right)\right] \cdot \frac{\rho_{snow}^i}{\rho_w} \cdot D_{snow}^i \qquad (23)$$

332 with $r_{min} = 0.03$, $r_{max} = 0.10$ and $\rho_t = 200$ kg m^{-3}.

333 Runoff (S_{melt}) is computed as the sum of meltwater produced at the surface and the total liquid water that has

334 percolated down to the bottom layer and that exceeds W_{max}^{bottom}. It is thus simply given by:

335 $$M_{snow} = \frac{\sum_i E_{snow}^i}{L_f} \qquad (24)$$

336 At each time step, changes in layer thickness, density and liquid water content in each layer are updated as well as

337 changes in snow temperature due to melting or refreezing. In case of complete snow melting, the energy excess

338 that has not been used for phase changes is used to warm the underlying ground.

2.2 New developments

2.2.1 New snow layering scheme

341 As mentioned in Section 1, snow models of intermediate complexity are a good compromise between detailed

342 snow models and single-layer models. They are designed to be implemented in ESMs and, as such, should not

343 require excessive computational time. Although their vertical resolution is generally limited to five layers at most

344 (Cristea et al., 2022), several studies reported that snow models of intermediate complexity considerably improve

345 the representation of basic features of the snowpack and reduce biases in surface temperature when they are

346 compared to single-layer models (Lynch-Stieglitz, 1994; Boone and Etchevers, 2001; Dutra et al., 2012; Wang et

347 al., 2013). Despite these good performances, increasing the number of snow layers (with finer layers near the

348 surface or near the snow/ice interface) is expected to improve the modeled heat conduction within the snowpack,

349 the simulated temperature at the snow/ice interface, and subsequently the vertical temperature profile in the ice

350 and eventually the simulated SMB (Cristea et al., 2022). We therefore increased the number of snow layers from

351 3 to 12, following the layering scheme proposed by Decharme et al. (2016) for ISBA-ES in which the new layering

352 scheme is defined as:

353
$$
\begin{cases}
D_{snow}^i = min\left(\delta_i, \frac{Z_{snow}}{12}\right) \; for \; i \leq 5 \; or \; i \geq 9 \\[8pt]
D_{snow}^6 = 0.3d_r - min(0, 0.3d_r - D_{snow}^5) \\[8pt]
D_{snow}^7 = 0.4d_r + min(0, 0.3d_r - D_{snow}^5) - min(0, 0.3d_r - D_{snow}^9) \\[8pt]
D_{snow}^8 = 0.3d_r - min(0, 0.3d_r - D_{snow}^9) \\[8pt]
d_r = Z_{snow} - \sum_{i=1}^5 D_{snow}^i - \sum_{i=9}^{12} D_{snow}^i
\end{cases}
\qquad (25)
$$

354 The δ_i values correspond to the maximum widths of the layers 1 to 5 and 9 to 12 and are fixed to $\delta_1 = 0.01$ m,

355 $\delta_2 = 0.05$ m, $\delta_3 = 0.15$ m, $\delta_4 = \delta_{10} = 0.5$ m, $\delta_5 = \delta_9 = 1$ m, $\delta_{11} = 0.1$ m, and $\delta_{12} = 0.02$ m. For very thin

356 snowpacks ($Z_{snow} \leq Z_{thin} = 0.1$ m), each layer has the same thickness $\frac{Z_{thin}}{12}$. The layer thicknesses are updated

357 at each time step if the first two layers (i = 1, 2) or the bottom layer (i = 12) become too thin

358 $\left(less \; than \; D_{snow}^i = 0.5 \times min\left(\delta_i, \frac{Z_{snow}}{12}\right)\right)$ or too thick $\left(larger \; than \; D_{snow}^i = 1.5 \times min\left(\delta_i, \frac{Z_{snow}}{12}\right)\right)$. In that

359 case, the snow mass and heat content are redistributed according to the new layering scheme. Otherwise, the layer

360   thicknesses at the current time step are kept to their previous values (i.e. at the previous time step). This allows to

361   maintain the density and thermal conductivity of fresh snow as long as the depth has not changed too much. This

362   enables the model to work more closely with more complex models in which new snow layers are associated with

363   a new snowfall event.

364   **2.2.2 Implementation of ice layers**

365   In case the snow mass has completely melted, ice melting occurs if the available energy is sufficient and contributes

366   to runoff. To account for the presence of ice below the snow layers, we implemented a new module in ORCHIDEE

367   to compute the heat diffusion and the vertical temperature distribution in the ice as well as the potential ice melting.

368   This module works in a similar way as the ES model and only accounts for vertical fluxes. The ice reservoir is

369   discretized into eight layers whose maximum thicknesses are fixed to 0.01, 0.05, 0.15, 0.5, 1, 5, 10 and 50 m. A

370   finer vertical spacing is imposed for the upper layers to better resolve heat conduction at the snow-ice or

371   atmosphere-ice interface. The large thickness of the bottom layer allows it to have an almost constant temperature

372   throughout the year as it has been observed at a few tens of meters depth (Patterson, 1994). Ice layers are only

373   implemented above an icy soil-type. If the icy soil is predominant in a given grid cell, then the entire surface

374   corresponding to this grid point will be considered as icy.

375   In the absence of a dynamic ice model that transports ice from the interior of the ice sheet (or glacier) to the edges,

376   the total ice mass may disappear entirely in the ablation zones especially in long-term simulations. To avoid such

377   situations, ice is considered as an infinite reservoir: melting ice contributes to runoff but, at each time step, the

378   amount of ice melted in the upper layers is counterbalanced by ice added at the base, and the layer thicknesses are

379   kept fixed to their initial value.

380   The vertical distribution of temperature is determined using the same numerical scheme as that for the snowpack.

381   If snow is still present over the ice soil, the temperature in the top ice layer is given by the temperature of the

382   bottom snow layer computed using Eq. (21). If snow has completely melted, the temperature in the first ice layer

383   is given by an expression similar to Eq. (20):

384    $$T_{ice}^1 = \left[\frac{\lambda_{ice} \cdot C_{gr\_ice} + (T_{surf} + T_{snow}^{add})}{1 + \lambda_{ice}(1 - D_{gr\_ice})} \right] \qquad (26)$$

385   For the deeper layers, the ice temperature is expressed as follows:

386    $$T_{ice}^{i+1} = C_{gr\_ice} + D_{gr\_ice} \cdot T_{ice}^i \qquad (27)$$

387   Similarly to the snow coefficients (see Eqs 20 and 21), λ_{ice}, C_{gr_ice}, D_{gr_ice} depend on the vertical discretization

388   and the thermal properties of the ice. The formulations of the heat capacity (C_{ice}) and thermal conductivity (Λ_{ice})

389   of the ice have been taken from those used in the GRISLI ice-sheet model (Yen, 1981) and are given by:

390    $$C_{ice} = \rho_{ice} \left(a_{ci} + b_{ci}(T_{ice} - T_0) \right) \qquad (28)$$

391    $$\Lambda_{ice} = a_{\lambda i} exp(b_{\lambda i} \times T_0) \qquad (29)$$

392   where T_{ice} is the ice temperature, a_{ci} = 2115.3 J K^{-1} kg^{-1}, b_{ci} = 7.79293 J K^{-2} kg^{-1}, $a_{\lambda i}$ = 6.727 W m^{-1} K^{-1} and $b_{\lambda i}$

393   = -0.041 K^{-1}.

394   A major difference between the hydrology of snow and ice layers lies in the fact that ice is considered as an

395   impermeable medium. Hence, liquid water coming from melting ice is considered to runoff instantaneously with

396   no possibility of refreezing. As a result, when the ice temperature is above the melting point, the available energy

397   for phase change in the ith ice layer (J m^{-2}) is given by:

398    $$E_{ice}^i = C_{ice}^i \left(T_{ice}^i - T_0\right) D_{ice}^i \tag{30}$$

399   Similarly to S_{melt} (Eq. 24), the total amount of ice melt is given by:

400    $$M_{ice} = \frac{\sum_i E_{ice}^i}{L_f} \tag{31}$$

401   and the runoff is computed as the sum of M_{snow} and M_{ice}. Given the fact that snow drift is ignored, the surface

402   mass balance is computed as:

403    $$SMB = P_{snow} + P_{rain} - M_{snow} - M_{ice} - S_{snow} \tag{32}$$

2.2.3 Other processes in the new ES model

405   Another modification made to the ES module concerns the inclusion of rainwater percolation within the snowpack

406   that may refreeze at depth as long as the maximum water holding capacity is not exceeded. In case of rain-on-

407   snow events, we also enhanced snow ageing by a factor of two ($f_{age} = f_{age}$ x 2). Although it sounds somewhat

408   arbitrary, we introduced this parameterization in the model to account for the effect of such events on

409   metamorphism and densification (Marshall et al., 1999), thereby lowering the albedo (Yang et al., 2023).

410   The snow thermal conductivity has been modified to follow a similar formulation to that used in the ISBA-ES

411   model (Decharme et al., 2016) and the CROCUS model (Vionnet et al., 2012) and earlier proposed by Yen (1981).

412   Therefore, the effective thermal conductivity in the ith layer now reads as:

413    $$\Lambda_{eff}^i = \left(a_{\lambda v} + \frac{b_{\lambda v}}{c_{\lambda v} + T_{snow}^i}\right)\frac{P_0}{P} + \Lambda_{ice}\left(\frac{\rho_s^i}{\rho_w}\right)^{1.88} \tag{33}$$

414   The first term of the right-hand side that parameterizes the water vapor diffusion effects (Λ_{vap}^i) remains unchanged

415   (see Eq. 15). The second term replaces Eq. (14) used in the previous ES version (Wang et al. 2013) and corresponds

416   to the new formulation of the snow thermal conductivity (Λ_{cond}^i). Here, the ice thermal conductivity (Λ_{ice}) differs

417   from the value found in Decharme et al. (2016) and is given by Eq. (29).

418   Besides the new snow layering scheme and the changes mentioned in this section, all the other processes simulated

419   in the new ES module are treated in the same way as in the three-layer version.

3. Experimental setup

3.1 Forcing by the regional atmospheric model MAR

422   The ORCHIDEE-ICE simulations presented in this paper were driven by the atmospheric outputs of the regional

423   atmospheric model MAR (Fettweis et al., 2017). This approach was motivated by the fact that MAR was initially

424   developed for polar regions (Gallée and Schayes, 1994). Moreover, it is coupled to a land surface scheme, SISVAT

425   (Soil Ice Snow Vegetation Atmosphere Transfer, De Ridder and Schayes, 1997), that includes a physically-based

426   snowpack model derived from the multi-layered snow model CROCUS (Brun, 1989, 1992). As such, MAR has

427   been extensively used to simulate the present-day climate and surface mass balance of the GrIS, and compares

428   well to reanalyses and available data of SMB measurements (e.g. Fettweis et al. 2017, 2020; Franco et al. 2012;

429 Montgomery et al. 2020; Delhasse et al., 2020). Therefore, the use of atmospheric forcings from MAR offers a
430 good opportunity to assess the performances of our snow model for simulating the SMB and ablation-related
431 processes.

432 The MAR simulations (1960 – 2019) were run at a 20 km x 20 km resolution. Here, we use the version v3.11.4,
433 identical to the version v3.11.5 for the Greenland ice sheet (Smith et al. 2023). MAR was forced every six hours
434 at its lateral boundaries by the meteorological fields (temperature, humidity, wind, and pressure) coming from the
435 ERA-40 (1960-1978, Uppala et al., 2005) and the ERA-Interim (1979-2019, Dee et al., 2011) reanalyses from the
436 European Centre for Medium-Range Weather Forecasts (ECMWF). Sea surface temperatures and sea ice cover,
437 also coming from ECMWF reanalyses, were 6-hourly prescribed.

438 **3.2. The ORCHIDEE-ICE simulations**

439 The ORCHIDEE-ICE simulations are run at a half-hourly time step with the same spatial resolution as the MAR
440 outputs (20 km x 20 km). The integration domain covers the whole of Greenland. ORCHIDEE-ICE is forced every
441 three hours by the downward shortwave and longwave radiation, the surface air temperatures and specific humidity
442 (all at 2 meters) and the wind speed (at 10 meters), the surface pressure and the precipitation rate (split between
443 rainfall and snowfall). Simulations are performed over the 1995-2019 period. The first five years (1995 to 1999)
444 are used for the initialization of the snowpack and are not included in the analysis. However, to obtain reasonable
445 thermal conditions within the ice layers, a longer time integration is required. Thus, we performed a preliminary
446 spin-up experiment over the same 25 years to infer an initial vertical temperature profile for the subsequent
447 ORCHIDEE-ICE simulations.

448 The name and the characteristics of the different experiments presented in this paper are summarized in Table A1.
449 Using the experimental design described above, we first ran the ES model with three and twelve snow layers (STD-
450 3L and STD-12L experiments respectively) to evaluate the added value of the new layering scheme. These
451 experiments were carried out with the albedo parameters used in the CMIP6 ORCHIDEE version (Chéruy et al.,
452 2020) and referred hereafter to as the standard snow albedo parameters.

453 Due to the strong sensitivity of the SMB to the albedo, we also conducted two additional experiments with
454 modified values of the albedo parameters. In the ASIM-12L experiment, we used the parameters inferred from the
455 approach of Raoult et al. (2023). This latter was based on a data assimilation experiment using the MODIS
456 retrievals. The main goal of their study was to optimise the albedo parameters so as to improve the albedo for the
457 ice sheet as a whole, while giving an extra weight to the edges where the greatest amount of runoff is produced.
458 In doing this, they also succeeded in improving the model-data fit between the ORCHIDEE albedo and MODIS
459 retrievals over the whole GrIS, and reducing the root-mean-square error (RMSE) by ~25 %. However, their work
460 was done with a previous version of the ORCHIDEE-ICE model with only three snow layers and in which the ice
461 layers were not implemented. Instead, ice was mimicked by a soil type whose porosity and volumetric water
462 content were set to 98% to simulate a soil filled with frozen water.

463 The logical follow-up to the work of Raoult et al. (2023) would have been to apply the optimisation algorithm to
464 the new version of ORCHIDEE-ICE. Since this approach is highly time-consuming, it has not yet been carried
465 out, albeit it will be the focus of further investigations. Therefore, using the new ORCHIDEE-ICE model version,
466 we adopted a manual tuning approach (i.e. trial-and-error method) to adjust the albedo parameters (OPT-12L
467 experiment). This procedure consists in 1/ changing the parameter values, the new value being taken from the

range reported in Table 1, 2/ running the model with the new parameter values, 3/ evaluating the model

performance (in terms of SMB and its components) using statistical criteria (e.g. RMSE between MAR and

ORCHIDEE-ICE) and 4/ repeating steps 1/ to 3/ until an acceptable calibration is obtained (i.e. acceptable values

of SMB, runoff, refreezing and sublimation).

Finally, to assess the impact of the climatic fields used as inputs of ORCHIDEE-ICE, we performed another

experiment (ERA5-12L experiment) by forcing the model with the ERA5 reanalysis (Hersbach et al., 2020) and

using the same albedo parameters than in OPT-12L experiment.

Table 1: List of the ORCHIDEE-ICE experiments (first column) with values chosen for the different albedo parameters (standard albedo parameters for STD-3L and STD-12L, optimized albedo parameters inferred from Raoult et al. (2023) for ASIM-12L and manual-tuned parameters for OPT-12L and ERA-12L. Values in brackets indicate for each parameter the range of values considered in the manual tuning approach.

Exp.	Nb of snow layers	A_{aged} [0.50 - 0.70]	B_{dec} [0.10 - 0.40]	τ_{dec} [1.0 - 10.0]	δ_c [0.2 - 2.0]	ω_1 [1.0 - 7.0]	$\omega2$ [0.5 - 6.0]	τ_{max} [40 - 60]	α_{ice} [0.30 - 0.50]
STD-3L	3	0.620	0.170	10	0.2	7	4	50	0.400
STD-12L	12	0.620	0.170	10	0.2	7	4	50	0.400
ASIM-12L	12	0.553	0.320	6.911	0.783	3.037	3.974	56.183	0.476
OPT-12L	**12**	**0.580**	**0.280**	**2.0**	**1.0**	**3**	**6**	**54**	**0.420**
ERA-12L	12	0.580	0.280	2.0	1.0	3	6	54	0.420

4. Methodology for the model performance evaluation

4.1 Comparison with MAR outputs

Our first objective is to assess the performance of the ORCHIDEE ICE model in representing the GrIS SMB. The

period under study spans over the 2000-2019 period. As mentioned in Section 3, MAR has revealed good

capabilities in simulating the SMB of present-day Greenland when compared to observational data. Therefore, at

the scale of the entire GrIS, our evaluation is made with respect to the MAR outputs (Figs 2a-5a). In all simulations

presented in this paper except ERA5-12L, the forcing fields of the ORCHIDEE-ICE model are provided by MAR

outputs. These include solid and liquid precipitation which constitute the accumulation (and the climatic)

component of the SMB. By using the MAR forcing, our analysis of the ability of ORCHIDEE-ICE to reproduce

ablation processes (runoff and sublimation) is made easier and is not biased by the use of another forcing.

4.2 Comparison with available data

In this study, we compared the albedo computed in ORCHIDEE-ICE with satellite-derived estimates of daily

albedo. We used Collection 6 from the MOD10A1 product (Hall et al., 1995) retrieved from the NASA space-

borne sensor MODIS. We chose this product because it has a good spatiotemporal coverage over snow-covered

areas. It is also one of the best performing products in terms of comparison with in situ data (Urraca et al., 2022,

2023). Moreover, while studies based on the previous Collection 5 reported deficiencies at latitudes higher than

70°N (Alexander et al., 2014), substantial improvements have been made to Collection 6 by using all available

observations for the acquisition period against only four observations per day in Collection 5 (https://lpdaac.usgs.gov/products/mcd43d11v006/, last access 01/22/2024). As a result, better quality retrievals are obtained at high latitudes despite a slight negative bias (Urraca et al., 2022). To avoid inaccuracies in retrieved data due to the presence of clouds or aircraft condensation trails, the MOD10A1 albedo product used in this study was further processed by Box et al. (2017): data have been de-noised, gap-filled, corrected for the sun-angle bias and validated using daily ground albedo values from the PROMICE (Programme for Monitoring of the Greenland ice sheet, Fausto et al., 2021) and GC-net automatic weather stations (Box et al. 2017).

We aggregated the albedo data (500 m x 500 m) onto the MAR grid to make the comparison between MODIS data and the ORCHIDEE-ICE outputs. In this study, we used the albedo data covering the 2000-2017 period because data for the years 2018 and 2019 were undefined. The resulting dataset may be used to calibrate the mean ORCHIDEE-ICE albedo, computed as the mean between the visible (from 0.4 to 0.7 μm) and near infrared (from 0.7 to 2.5 μm) bands (see Section 2).

As in Fettweis et al. (2020), we also evaluated the modelled SMB with the Machguth et al. (2016) SMB database. Daily outputs are used here over 2000-2019. Modelled SMB were linearly interpolated to the measurement point location and corrected for the elevation difference between the MAR native topography at 20km and the one provided in the SMB database. This was done by using a space-varying SMB–elevation gradients, as proposed by Franco et al. (2012) and Noël et al. (2016). Finally, measurements not included in the 2000–2019 period and records located outside the 20km MAR ice mask are discarded from the evaluation.

4.3 Statistical metrics

To evaluate our model performances, we used statistical metrics:

The root-mean-square error (RMSE) has been computed using the monthly mean variables averaged over 2000-2019 for the SMB and its components, and over 2000-2017 for the albedo. It is defined as:

$$RMSE = \sqrt{\frac{1}{N}\sum_{i=1}^{N}(X_{OR}(i) - X_{MAR}(i))^2} \tag{34}$$

where $X_{OR}(i)$ and $X_{MAR}(i)$ represent the ORCHIDEE-ICE and the MAR variables respectively at each grid point i, N is the number of unmasked grid points (i.e. related only to the ice-covered area) and i stands for the ith grid point. The RMSE is a metric widely used to compare different models but it has some shortcomings related to the fact that higher weights are given to larger errors. We there used additional statistical criteria to provide a more in-depth picture of our analysis. We computed the spatial RMSE (SRMSE) which gives a measure of the quadratic difference averaged over time between values simulated by both models over the entire GrIS domain and at each time step. Thus, by taking the temporal variations in the simulated time series into account, the spatial RMSE makes it possible to assess the model's performance both over the entire geographical domain and over the time period under consideration. It is computed as follows:

$$SRMSE = \sqrt{\frac{1}{N_t \times N} \sum_{t=1}^{N_t}\sum_{i=1}^{N}(X_{i,OR}(t) - X_{i,MAR}(t))^2} \tag{35}$$

529    $X_{i,OR}(t)$ and $X_{i,MAR}(t)$ are respectively the ORCHIDEE-ICE and MAR variables at each grid point i and each time

530   step t. N_t is the number of time steps. In contrast to the RMSE, we used the daily simulated values to compute the

531   SRMSE.

532   While the RMSE and SRMSE give an indication of the magnitude of the absolute difference between both models,

533   it is also important to calculate the area-weighted average bias (hereafter, areal-mean bias) of each grid point in

534   order to examine whether the model variables simulated by ORCHIDEE-ICE are underestimated (negative bias)

535   or overestimated (positive bias). This bias (MB) is given by:

536    $$MB = \frac{\sum_{i=1}^{N} A_i(X_{OR}(i) - X_{MAR}(i))}{\sum_{i=1}^{N} A_i}$$ (36)

537   where A_i is the surface area of each grid point.

538   Finally, we also examined the probability density functions (PDFs) and performed a Cramer-von Mises (CVM)

539   test (Anderson, 1962) to compare the MAR and ORCHIDEE-ICE distributions of a given variable. The CVM test

540   integrates the quadratic differences between the two models over the whole distributions (including the tails of the

541   distributions). In this sense, it is more powerful and more sensitive to departures from the reference distribution

542   (i.e. MAR) than the widely used Kolmogorov-Smirnov test (Stephens, 1970), which is based on the absolute value

543   of the greatest distance between the two distributions.

544   **5. Results**

545   **5.1 Evaluation against MAR for standard albedo parameters**

546   Figures 2 to 4 display the spatial distribution of runoff, sublimation and refreezing simulated by MAR (panels a)

547   and by ORCHIDEE-ICE in the STD-3L (panels b) and STD-12L (panels c) experiments. The main runoff areas

548   simulated with MAR are located on the western edge albeit, to some extent, runoff occurs in all peripheral areas

549   of the ice sheet (Fig. 2a). Locations of the ablation zones are well represented in ORCHIDEE-ICE but are limited

550   to a very narrow band, especially in the STD-3L simulation (Fig. 2b). Increasing the number of snow layers favors

551   the inland expansion of the ablation areas on the western and northern margins (Fig. 2c). However, this expansion

552   remains too restricted compared to MAR (Fig. 2a). In the ablation areas, differences in the amount of runoff exceed

553   1.5 mm day^{-1} (Fig. S1). Integrated over the whole ice sheet (Table 2), the runoff values computed in STD-3L (152

554   Gt yr^{-1}) and STD-12L (205 Gt yr^{-1}) experiments for the 2000-2019 period are respectively 59 % and 45 % lower

555   compared to MAR (375 Gt yr^{-1}). As a consequence of the considerably smaller amount of runoff in ORCHIDEE-

556   ICE, and thus of surface meltwater, refreezing is also much lower (Table 2) and less extended (Figs. 3a-c)

557   compared to MAR. It can be noted, however, that the disagreement is less pronounced with the STD-12L

558   experiment (Fig. S2), which underlines the benefit of increasing the number of snow layers.

559

Runoff 2000-2019 (mm day^{-1})
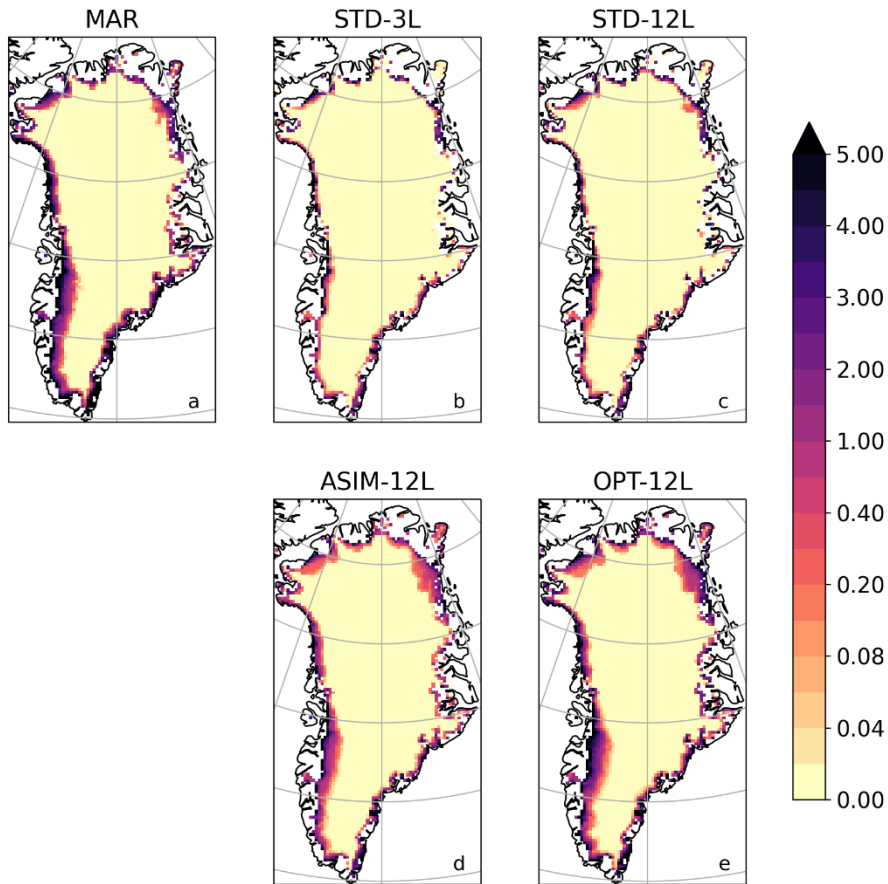
Figure 2: Spatial distribution of the runoff (in mm day^1) averaged over the 2000-2019 period and simulated with MAR (a) and the ORCHIDEE-ICE model (b-e) using: the three-layer snow scheme and the standard albedo parameters (b), the twelve-layer snow scheme and the standard albedo parameters (c), the twelve-layer snow scheme and the albedo parameters optimised using a data assimilation technique (Raoult et al., 2023) and a previous version of the ORCHIDEE-ICE model (d), the twelve-layer snow scheme and the albedo parameters obtained after manual tuning (e).

Table 2: Simulated values of SMB, runoff, sublimation and refreezing integrated over the entire Greenland ice sheet and averaged over the 2000-2019 period (2nd column). Evaluation of simulated SMB and SMB components is done with respect to MAR outputs using values of root-mean-square error (3rd column), areal mean bias and (4th column) and spatial root-mean-square error (5th column).

Experiments	SMB (Gt yr⁻¹)	RMSE (in mm day⁻¹)	Areal mean bias (in mm day⁻¹)	Spatial RMSE (in mm day⁻¹)
MAR	**286**			
STD-3L	504	0.976	0.351	3.050
STD-12L	450	0.786	0.264	2.809
ASIM-12L	466	0.706	0.290	2.602
OPT-12L	**301**	**0.464**	**0.024**	**2.530**
ERA5-12L	352			
Experiments	Runoff (Gt yr⁻¹)	RMSE (in mm day⁻¹)	Areal mean bias (in mm day-1)	Spatial RMSE (in mm day⁻¹)
MAR	**375**			
STD-3L	152	1.107	- 0.357	3.157
STD-12L	205	0.922	- 0.272	2.900
ASIM-12L	217	0.829	- 0.254	2.639
OPT-12L	**336**	**0.592**	**-0.063**	**2.539**
ERA5-12L	273			
Experiments	Sublimation (Gt yr⁻¹)	RMSE (in mm day⁻¹)	Areal mean bias (in mm day⁻¹)	Spatial RMSE (in mm day⁻¹)
MAR	**82**			
STD-3L	32	1.000	- 0.081	0.200
STD-12L	33	0.096	- 0.079	0.203
ASIM-12L	5	0.134	- 0.124	0.226
OPT-12L	52	0.077	- 0.049	0.274
ERA5-12L	89			
Experiments	Refreezing (Gt yr⁻¹)	RMSE (in mm day⁻¹)	Areal mean bias (in mm day-1)	Spatial RMSE (in mm day⁻¹)
MAR	**186**			
STD-3L	72	0.336	- 0.183	1.254
STD-12L	104	0.269	-0.131	1.134
ASIM-12L	90	0.313	- 0.155	1.182
OPT-12-L	**158**	**0.240**	**-0.046**	**1.316**
ERA5-12L				
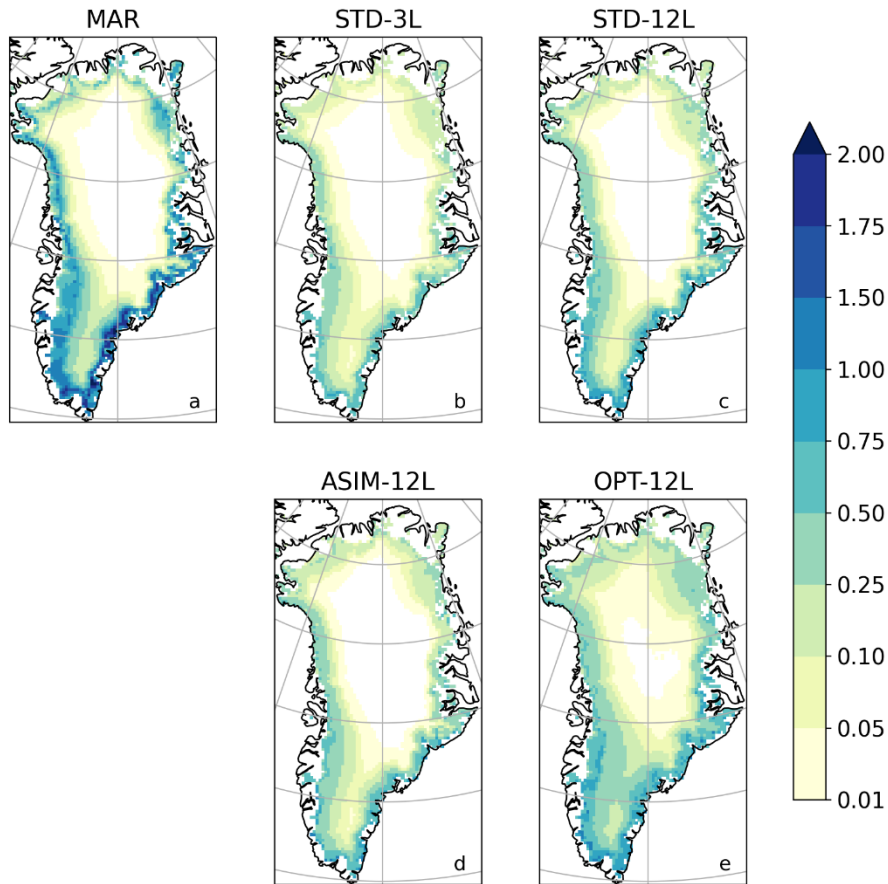
Figure 3: Same as Figure 2 for the simulated refreezing (in mm day⁻¹).

Large differences between MAR and ORCHIDEE-ICE also arise regarding sublimation (32 and 33 Gt yr⁻¹ in the STD-3L and STD-12L experiments respectively, against 82 Gt yr⁻¹ for the 2000-2019 period in MAR). This feature concerns the entire ice sheet but is even more striking in peripheral areas (Figs 4 and S3). In central Greenland, differences are smaller, but ORCHIDEE-ICE simulates a little condensation (Fig. 4) whereas MAR does not.

The differences in simulated runoff and in sublimation between MAR and ORCHIDEE-ICE translate into overestimated SMB values simulated with ORCHIDEE-ICE (504 and 450 Gt yr⁻¹ in STD-3L and STD-12L against 286 Gt yr⁻¹ in MAR; see also Figs. 5 and S4). Since inland regions are dominated by the accumulation signal, which is provided by the MAR outputs, the SMB anomalies are primarily driven by differences in the ablation components occurring at the edges of the ice sheet, and exceed 2 mm day⁻¹ in most parts of the western and southeastern margins.

An important conclusion that can be drawn from these results is that the use of a better resolved snow layering scheme (twelve-layer as opposed to a three-layer snow scheme) reduces the mismatch between MAR and ORCHIDEE-ICE. This is mainly illustrated by the integrated SMB and runoff values which are respectively ~35% lower and ~11% higher in STD-12L, translating into reductions of RMSE values (~19% and ~17% for SMB and runoff respectively, see Table2), areal mean bias (~25% and ~24% respectively), and, to a lesser extent, of the spatial RMSE (~8% for both SMB and runoff). Nevertheless, the differences with MAR are still too large for the model to be used as a reliable tool to compute the GrIS SMB.
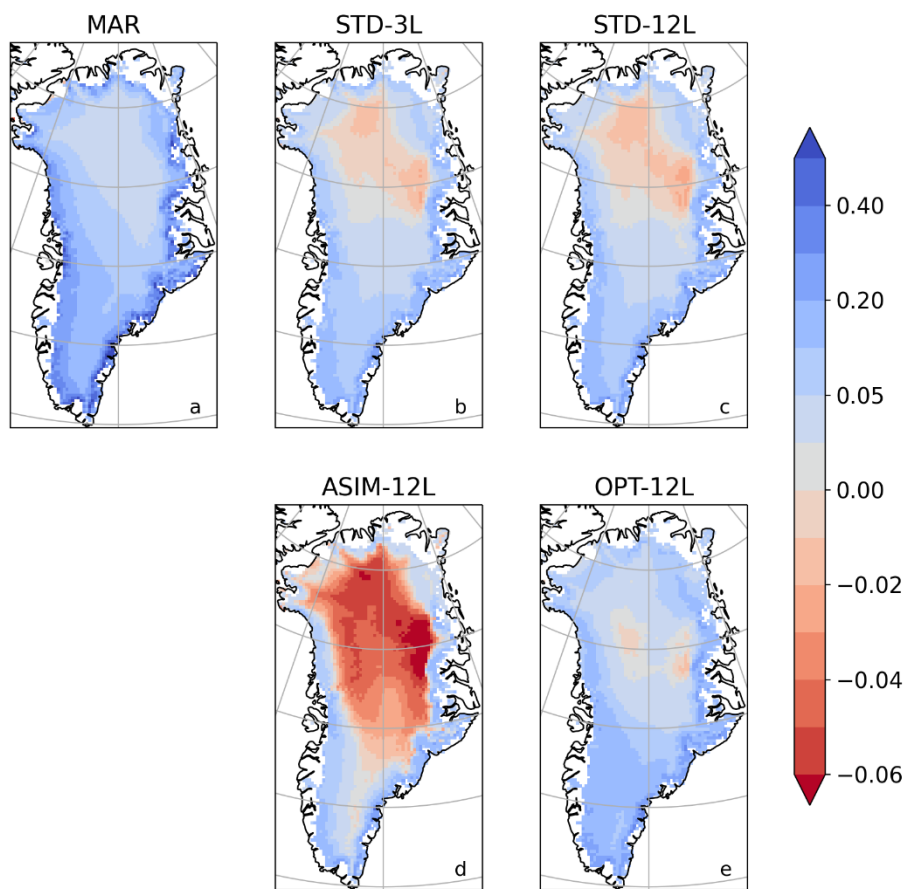
594

595 **Figure 4:** Same as Figure 2 for the simulated sublimation (in mm day⁻¹). Negative values indicate condensation.

596

597
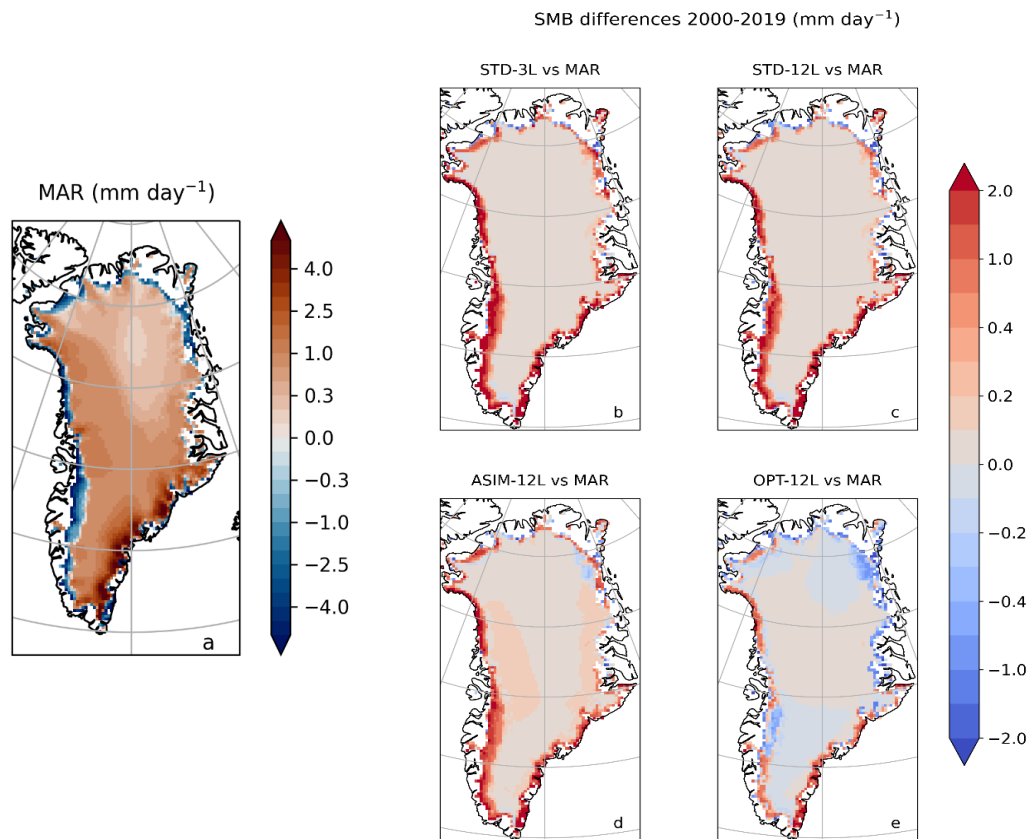
Figure 5: Spatial distribution of the GrIS SMB simulated with MAR (in mm day^{-1}) and averaged over the 2000-2019 period (a) Differences in the GrIS surface mass balance between MAR and the ORCHIDEE-ICE model (b-e) with the standard parameter values of the albedo parameterisation and the three-snow layering scheme (b). Panels (c-e) correspond to simulations performed with the updated twelve-snow layering scheme for standard values of the albedo parameters (c), optimised values of the albedo parameters (d), values of the albedo parameters obtained after manual tuning (e).

5.2. SMB and runoff for modified albedo parameters

5.2.1 Impact of optimised albedo parameters

As snow is a highly reflective medium, little changes in albedo may produce large changes in the surface energy balance, and thus, in the SMB. In the GrIS interior, there is generally a quite good agreement between the summer albedo computed by MAR and the standard ORCHIDEE-ICE simulations (i.e. STD-3L and STD12-L experiments, Figs. 6b and 6c and S5) with slight negative anomalies of less than 0.05. Negative anomalies (~ -0.1) also appear, mainly in the northern part of the ice sheet, but with only little consequences on surface melting owing to the very cold conditions in this region. However, on the western margin, where most of the melting takes place, larger snow albedo values are found in ORCHIDEE-ICE. This leads to underestimated surface temperatures compared to MAR (Fig. 7) and, thus, to undervalued runoff that may explain part of the discrepancies between MAR and ORCHIDEE-ICE. There are also differences between the observations provided by MODIS retrievals and the MAR albedo (Figs. 6a and 6f), especially in the northern and southern parts, and the western margin. On the other hand, the summer albedo computed in the STD-3L and STD-12L experiments (Figs. 6g and 6h) are generally too low in the interior of the ice sheet, and too high on the western margin with differences from 0.05 to 0.15.

618
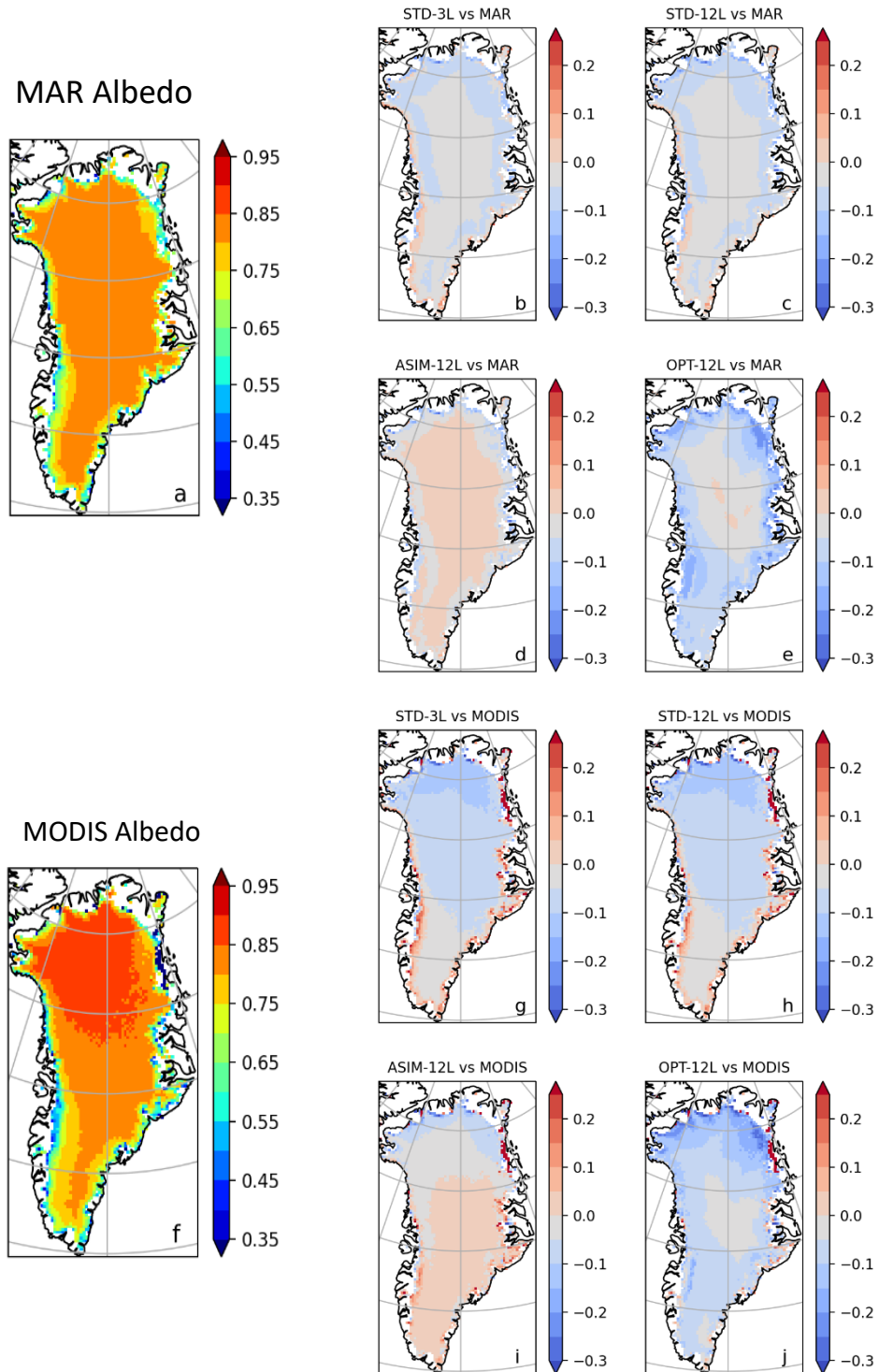
Figure 6: Left: Spatial distribution of the summer (JJA) albedo computed with MAR (a) and MODIS (f) and
averaged over the 2000-2017 period. Right: Differences between the albedo computed with ORCHIDEE-ICE and
MAR (b,c,d,e) and between ORCHIDEE-ICE and MODIS (g,h,i,j) for the three-layer snow scheme and the
standard albedo parameters (b,g), the twelve-layer snow scheme and the standard albedo parameters (c,h), the
albedo parameters inferred from a data assimilation technique and using a previous version of the ORCHIDEE-
ICE model (d,i), the albedo parameters obtained after manual tuning (e,j).

As mentioned in Section 3.2, we investigated the sensitivity of the SMB and its components to the albedo. We first performed an ORCHIDEE-ICE experiment (ASIM-12L) with the optimised albedo parameters inferred from Raoult et al. (2023). Figure 6i illustrates how the representation of the albedo has been improved in the ASIM-12L experiment compared to STD-12L (Figs. 6h, S5 and S8). Model-data discrepancies are now reduced with differences lower than 0.05 except in the northernmost parts of the ice sheet. The RMSE decreased by ~26% (Table 3), which is quite consistent with Raoult et al. (2023). The ablation areas are now better represented (Fig. 2d) due to increased surface temperatures (Fig. 7c) as a result of lower albedo values on the western margin (Fig. 6i).

Table 3: Albedo RMSE values (2nd column), areal mean biases (3rd column) and spatial RMSE with respect to MODIS (top) and MAR (bottom).

Experiments	RMSE (w.r.t MODIS)	Areal mean bias (w.r.t MODIS)	Spatial RMSE (w.r.t MODIS)
MAR	0.076	- 0.005	
STD-3L	0.098	- 0.047	0.098
STD-12L	0.097	- 0.051	0.097
ASIM-12L	0.072	0.001	0.072
OPT-12L	0.111	- 0.008	0.092
Experiments	RMSE (w.r.t MAR)	Areal mean bias (w.r.t. MAR)	Spatial RMSE (w.r.t MAR)
STD-3L	0.055	- 0.042	0.055
STD-12L	0.058	- 0.047	0.058
ASIM-12L	0.051	0.006	0.040
OPT-12L	0.092	- 0.047	0.092

However, despite the smaller mismatch between modeled ASIM-12L albedo and MODIS retrievals and the better representation of the ablation areas, the simulated amount of runoff (217 Gt yr^{-1}) integrated over the whole GrIS has been only slightly improved with respect to STD-12L (Figs. 2d) and remains quite different from MAR outputs (Figs. 2a). In addition, the simulated SMB (466 Gt yr^{-1}) has even been slightly degraded (Figs. 5a and 5d) due to negative temperature anomalies in central Greenland extending until the southern tip (Fig. 7c) resulting from slightly higher albedo values compared to MAR and MODIS (Figs 6a, 6i).

Figure 7: Spatial distribution of the snow temperature differences with respect to MAR averaged over the 2000-2019 period (in °C) simulated for the STD-3L (a), STD-12L (b), ASIM-12L (c) and OPT-12L (d) experiments.

The low performance for the SMB computation in ASIM-12L is not solely due to a small amount of runoff but also to strong negative values of sublimation (i.e. large condensation) over central Greenland (Fig. 3d) resulting in an average level of - 5 Gt yr^{-1} over the entire ice sheet compared to 82 Gt yr^{-1} in MAR (Table 2). In the ASIM-12L experiment, the albedo in the central GrIS region is slightly higher (up to 0.05) than the albedo retrieved from MODIS (Fig. 6i), while the albedo computed with MAR is slightly lower (Figs. 6a and 6f). This explains why the ASIM-12L surface temperatures are smaller than those simulated with MAR. This can lead, therefore, to lower saturation pressures that can drop below the dew point and thus produce solid condensation. This result highlights the key influence of the albedo on surface processes and, in particular, illustrates how a small departure from observations may lead to strong biases in sublimation estimates.

5.2.2 Manual tuning

As mentioned in Section 3, we have not yet performed a data assimilation experiment to calibrate the new twelve-layer ES model, given the computational cost of such an experiment. Instead, we chose to follow a trial-and-error approach. As runoff dominates the SMB signal, our primary objective was to improve the runoff computation by reducing the summer albedo values in the main ablation areas (i.e. the western margin). Given the number of albedo parameters, several options are available to achieve this:

- lowering the albedo of aged snow (A_{aged}) and/or the albedo of fresh snow ($A_{aged} + B_{dec}$);
- modifying the parameter controlling the decay rate of snow albedo (τ_{dec});

- increasing snow age by changing the parameters related to snow aging: the minimum snowfall thickness to reset snow age to zero (δ_c), the tuning parameters ω_1, ω_2 (see Eq. 10) and the maximum snow age (τ_{max});
- changing the ice albedo (α_{ice}) because it can also affect SMB and runoff computation if the snowpack melts entirely during summer months in some places and give rise to bare ice.

Owing to the various influences of the albedo parameters, we had to find a compromise so as to lower the albedo in ablation areas and improve the computation of runoff and SMB, while keeping reasonable albedo values in the GrIS interior. Among the values we tested for each of the parameters, the set of parameters providing the best agreement with MAR outputs (for SMB and SMB components) is highlighted in bold in Table 1 (OPT-12L experiment). Compared to the ASIM-12L experiment (Figs. 6i, S5, S8), the albedo mismatch between ORCHIDEE-ICE (OPT-12L experiment) and MODIS is amplified, especially along the western margin and in the northern sector with differences reaching 0.25 and 0.3 respectively (Fig. 6j). Nevertheless, these results were expected since our manual tuning was designed to increase the magnitude of the ablation components (especially runoff) and to decrease the SMB, and therefore to lower the albedo values with a direct impact on surface temperatures, hence surface melting and sublimation.

5.2.3 Impact on SMB components

Using the new set of albedo parameters obtained with the manual tuning approach, the ablation areas are now much more extended than those simulated in the STD-12L experiment (Figs. 2c and 2e). Compared to MAR (Fig. 2a), they are even wider in the northern part due to increased surface temperatures (Fig. 7d) in response to lower albedo values (up to -0.25). The total amount of runoff averaged over the 2000-2019 period is now 336 Gt yr^{-1} (against 375 Gt yr^{-1} in MAR). For the OPT-12L experiment, the RMSE value decreased by ~40% compared to STD-12L (Table 2). In the same way, the sublimation (52 Gt yr^{-1}) and refreezing (158 Gt yr^{-1}) better match with MAR (Table 2). In particular, condensation over central Greenland has been considerably reduced, notably with respect to ASIM-12L, but sublimation is still underestimated along the GrIS edges and in the southern part (Fig. 4e). The increase in refreezing (with respect to STD-12L and ASIM-12L) in the GrIS interior (Fig. 3e) is likely linked to lower summer albedo values (Figs. 6e and 6j) leading to a smaller amount of melting compensated by refreezing. In the main ablation areas, a larger refreezing is produced and thus a better agreement with MAR, though still insufficient, is obtained.

These results for the SMB components are evidently associated with an improved representation of the SMB itself (Fig. 5e) which now reaches 301 Gt yr^{-1} (286 Gt yr^{-1} obtained with MAR. Indeed, the RMSE and the spatial RMSE values have been reduced by ~41% and 10% respectively for the SMB (~28% and 9% for the runoff) compared to the STD-12L experiment (Table 2). An even more striking result concerns the areal mean bias which has been lowered by one order of magnitude. These improvements are also illustrated in Figure 8, which displays the monthly mean values for each grid point of the SMB components simulated with ORCHIDEE-ICE as a function of the same MAR variables (see for example the correlation coefficient for both SMB and runoff for the OPT-12L experiment). However, our results are less conclusive for sublimation and refreezing. Although, the areal-mean bias and the RMSE values indicate a better match between the OPT-12L and the MAR simulations, the spatial RMSE values are greater compared to the three other ORCHIDEE-ICE experiments, suggesting a lower temporal consistency between OPT-12L and MAR. In addition, the correlation coefficients for sublimation and refreezing

701 are also smaller (Fig. 8). On the other hand, the best overlaps between the probability density functions between

702 MAR and the ORCHIDEE-ICE experiments is undoubtedly obtained for OPT-12L, as shown in Figs. S6-S7 and

703 the scores of the CVM tests reported in Table S1.

704
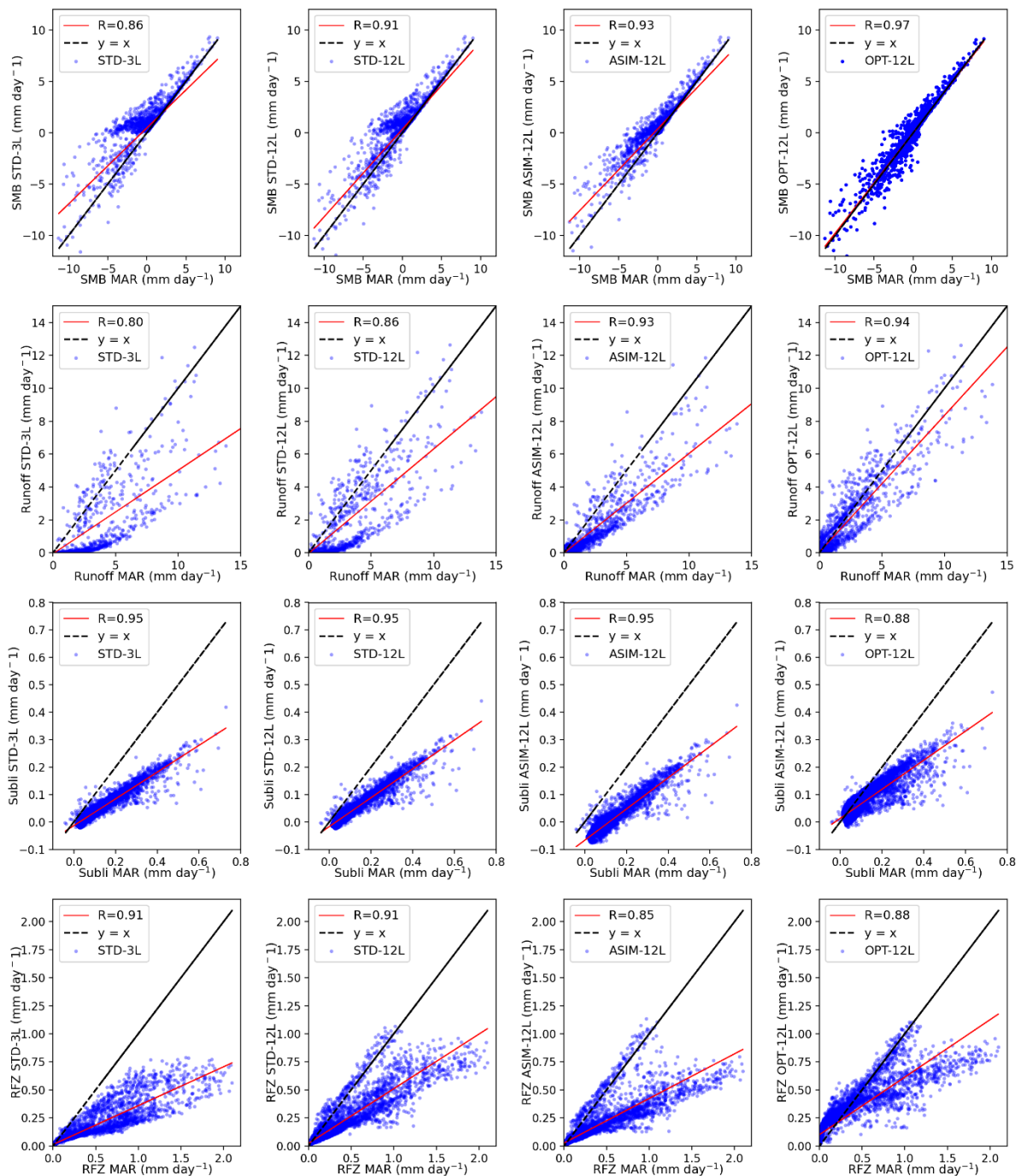
Figure 8: Representation of the simulated SMB (1st row), runoff (2nd row), sublimation (3rd row) and refreezing
(4th row) simulated with ORCHIDEE-ICE as a function of the same MAR variables: STD-3L (1st column), STD-12L (2nd column), ASIM-12L (3rd column) and OPT-12L (4th column). The different points represent the monthly mean values over the period 2000-2019 for each of the grid points. The regression line is displayed in red (R is the regression coefficient) and the line y = x is in black.

710 Despite these encouraging results, it is important to underline that the improved SMB simulation in OPT-12L is
711 achieved through the albedo reduction, and therefore, to some extent, come from error compensation. However,
712 the reduced albedo also makes it possible to compensate for the effect of some missing mechanisms, such as the
713 lack of consideration of snow-atmosphere interactions or the absence of an explicit representation of snow
714 metamorphism, which has a direct impact on the density profile, the albedo itself and the temperature profile.

5.3 Vertical temperature and density profiles

716 To go a step further and gain a better understanding of the above results, it is also important to explore the internal
717 processes of the snowpack. To achieve this, we chose to focus on the vertical temperature and density profiles.
718 Figure 9 depicts the snow temperatures simulated ORCHIDEE -ICE as a function of the MAR snow temperatures
719 at 20 cm and 1 m depth of the snowpack. These plots show that the temperatures simulated in STD-3L, STD-12L
720 and OPT-12L behave approximately in the same way when compared to those of MAR. In the first 20 cm,
721 ORCHIDEE-ICE is slightly warmer than MAR for temperatures between -30°C and -10°C, despite a few slightly
722 colder grid points appearing in the range of -20°C to -10°C. The ASIM-12L experiment presents the best agreement
723 with MAR, although slightly lower temperatures. These features reflect directly the behavior of surface
724 temperatures (Fig. 7) that strongly influence the upper snowpack layers. Another key point arising from these plots
725 is the very good agreement between MAR and ORCHIDEE-ICE for temperatures above -10°C. This suggests that
726 the potential runoff that could occur in the first tens of centimeters of the snowpack should not be so much affected.
727 However, the departure from MAR increases with snow depth, especially for low temperatures. For example, at
728 1 m depth, differences of 3-4°C are obtained (Fig. 9) and may exceed 5°C for deeper levels (not shown). These
729 enhanced differences with MAR are likely due to a positive feedback related to the thermal conductivity (see Eq.
730 33): As snow temperature increases by 1°C in a given layer, the thermal conductivity increases by one order of
731 magnitude.

732 As pointed out by Domine et al. (2019), the snow thermal regime and snow density are strongly coupled. As an
733 example, they mentioned the work of Fréville (2015) who showed that an error of 1°C in the surface temperature
734 can lead to errors on snow density of 100 kg m^{-3}. Our experiments show that for a depth of 20 cm, the higher the
735 surface temperature, the lower the snow density on average (Fig. 10). On the other hand, in the ASIM-12L
736 experiment, snow temperatures are lower, compared to the three other ORCHIDEE-ICE experiments, and snow
737 densities are larger. This contradicts a number of studies (e.g. Kojima, 1967; Anderson 1976, Mizukami and Perica,
738 2008), which have shown that in a warmer snowpack, snow grains become rounded and are more prone to be
739 compacted more easily, hence leading to an increase in snow density. However, in our model this process cannot
740 be reproduced as snow metamorphism is only accounted for through snow ageing. Conversely, in deeper layers,
741 the model is more effective at densifying (Fig. 10), in line with the fact that warmer snow becomes more plastic
742 and compacts more easily. In particular; between 20 cm and 1 m depth, the RMSE computed between OPT-12L
743 and MAR has been reduced from 79.63 kg m^{-3} to 30.22 kg m^{-3}. Beyond 600 kg m^{-3}; the ORCHIDEE-ICE densities
744 are generally below those of MAR because the maximum density is fixed to 750 kg m^{-3} (see Section 2). However,
745 the comparison of our results on snow density with those of MAR should be viewed with caution because, to the
746 best of our knowledge, the snow density simulated by MAR has not been evaluated against available observations.

747

Snow Temperature 2000-2019 (°C)
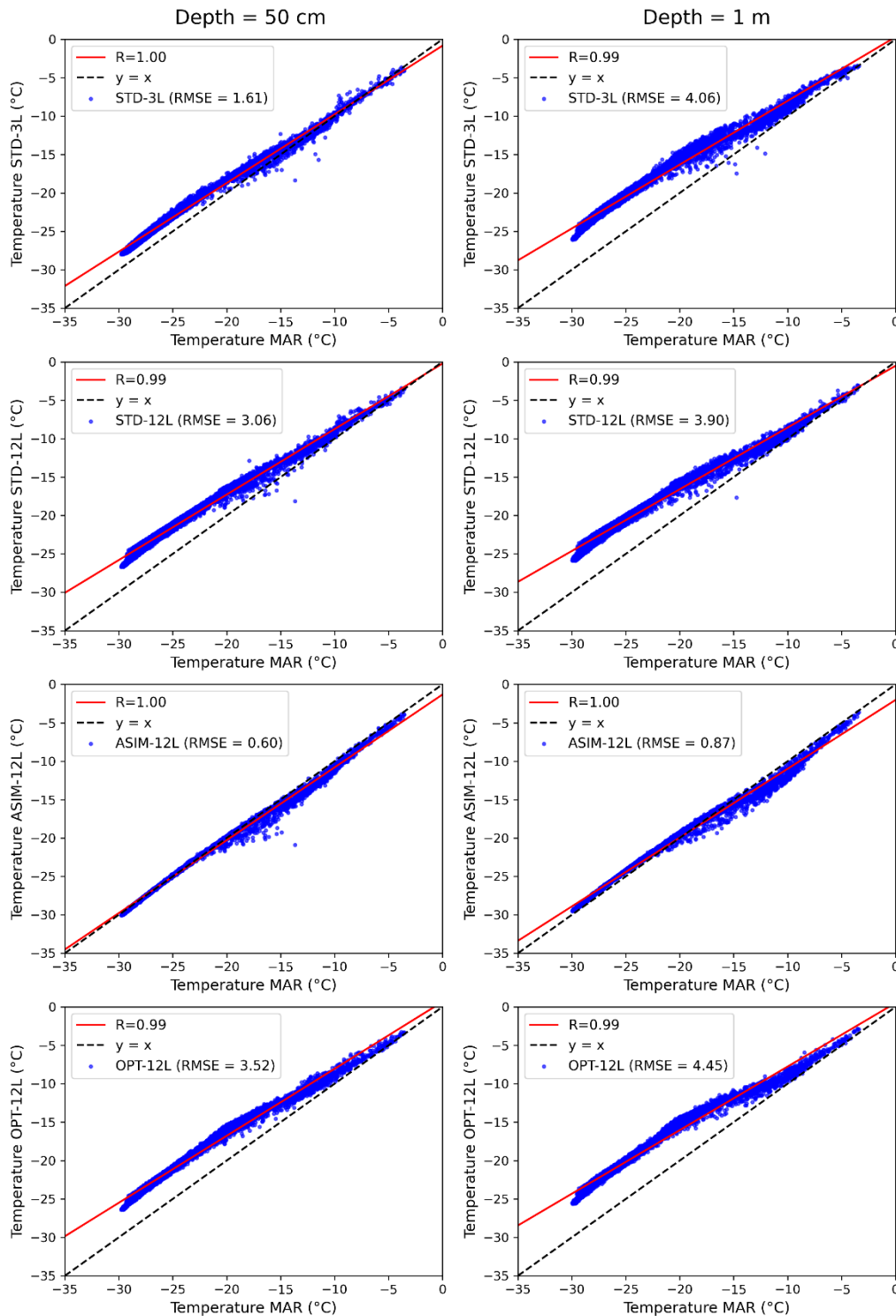
Figure 9: Representation of the ORCHIDEE-ICE simulated snow temperatures at 50 cm (left) and one-meter depth (right) as a function of the MAR snow temperatures. The different points represent the monthly mean values over the period 2000-2019 for each grid point. The regression line is displayed in red (R is the regression coefficient) and the line y = x is in black.

753

754
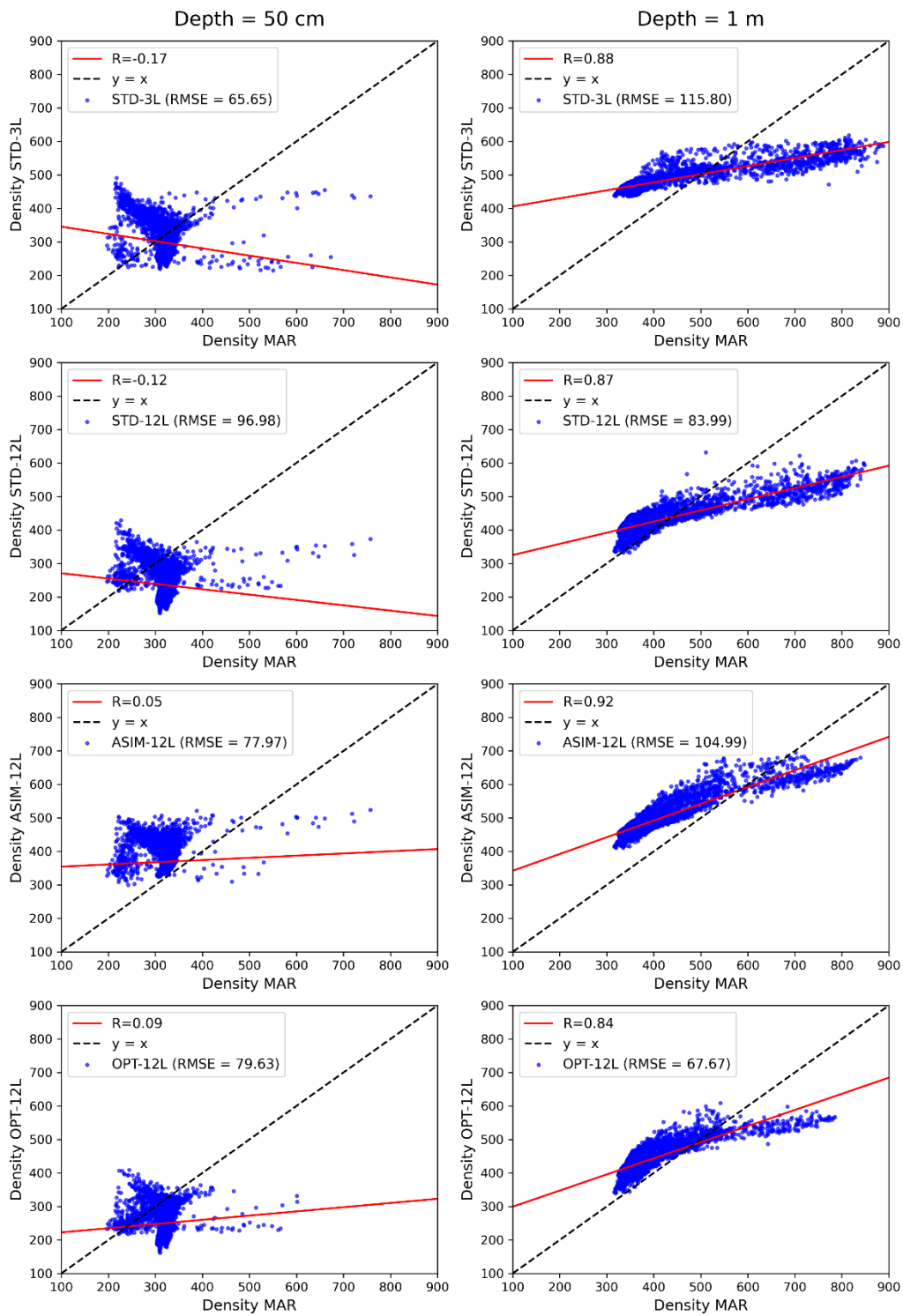
Figure 10: Same as Figure 9 for snow density

756

757

5.4 SMB evolution: impact of the climate forcing

The results presented in the previous sections were averaged over the 2000-2019 period (for SMB and the SMB components) and over the 2000-2017 period (for the albedo). In this part, we present the temporal evolution of the SMB between the years 2000 and 2019 (Fig. 11). Figure 11 shows that whatever the ORCHIDEE-ICE experiment under consideration, the evolution of the yearly integrated SMB is in accordance with the evolution simulated by the MAR model. In particular, the years in which extreme melting events were recorded (such as 2012 and 2019) are perfectly well represented (Bennartz et al. 2013; Tedesco and Fettweis 2020). As expected, the best agreement with MAR is obtained for the OPT-12L experiment as a result of the calibration of the albedo parameters. When forced by the ERA-5 meteorological fields, and using the manually-tuned parameters, ORCHIDEE-ICE simulates higher SMB values and a lower runoff (Fig. 11 and Table 2), especially during the first period of the time series (2000-2008). However, the evolution of the yearly integrated SMB in the ERA5-12L experiment follows exactly the same interannual variations as for the OPT-12L experiment forced with MAR (Fig. 11). This indicates that the surface climate simulated by MAR is close to that derived from the ERA-5 products. Moreover, in a comparative study of the ERA-5 reanalyses, Arctic System reanalysis and MAR performances, Delhasse et al. (2020) showed that MAR outperforms ERA-5 for the near-surface temperatures when compared to observations from automatic weather stations. As the surface melt, and thus the SMB, largely depend on near-surface temperatures, there is, therefore, a strong interest in using MAR to force our snow model and to compare its performances to those of MAR.
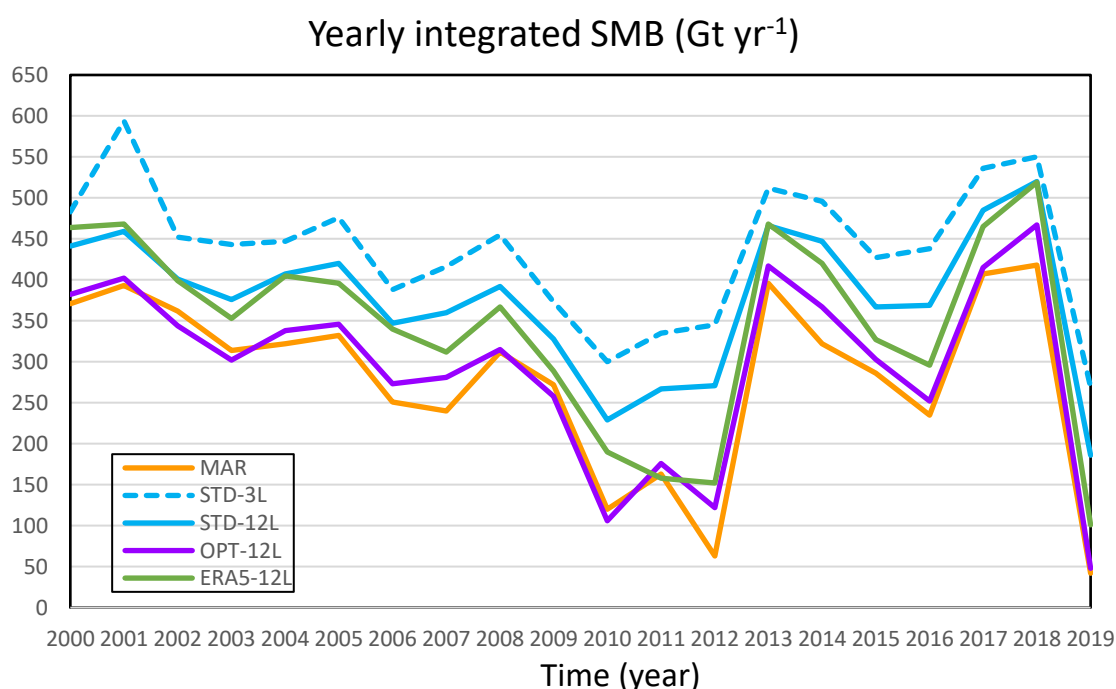
Figure 11: Evolution of the yearly surface mass balance of the Greenland ice sheet simulated with MAR (black), ORCHIDEE-ICE forced by MAR outputs (STD-3L and STD-12L: yellow, solid and dashed lines respectively; OPT-12L: red line), ORCHIDEE-ICE forced by the ERA-5 reanalyses (green line).

781   In this paper, we have so far limited the comparison of our results to those of MAR. However, as mentioned in

782   Section 4, we also evaluated the simulated SMB with 353 daily SMB observations from the PROMICE database

783   available over the 2000-2019 period (Machguth et al., 2016; Mankoff et al., 2021). In addition, it is also interesting

784   to evaluate our model results against observations when ORCHIDEE-ICE is forced by climatic fields independent

785   from MAR outputs. To address this issue, we plotted the modelled SMB for OPT-12L, ERA5-12L and MAR for

786   the grid points located closest to the observation sites as a function of the PROMICE SMB measurements (Fig. 12).

787   We also provided statistical elements for the comparison between MAR, the five ORCHIDEE-ICE

788   experiments and the SMB observations (Table 4). This model-data comparison confirms the conclusions we

789   reached when evaluating the performance of our model against MAR outputs, namely the significant improvement

790   in our results when moving from STD-3L to OPT-12L. Moreover, although the bias between the OPT-12L SMB

791   and the observed SMB is twice as high as for MAR, the model-data correlation is of the same order of magnitude

792   as for MAR (Table 4).

793
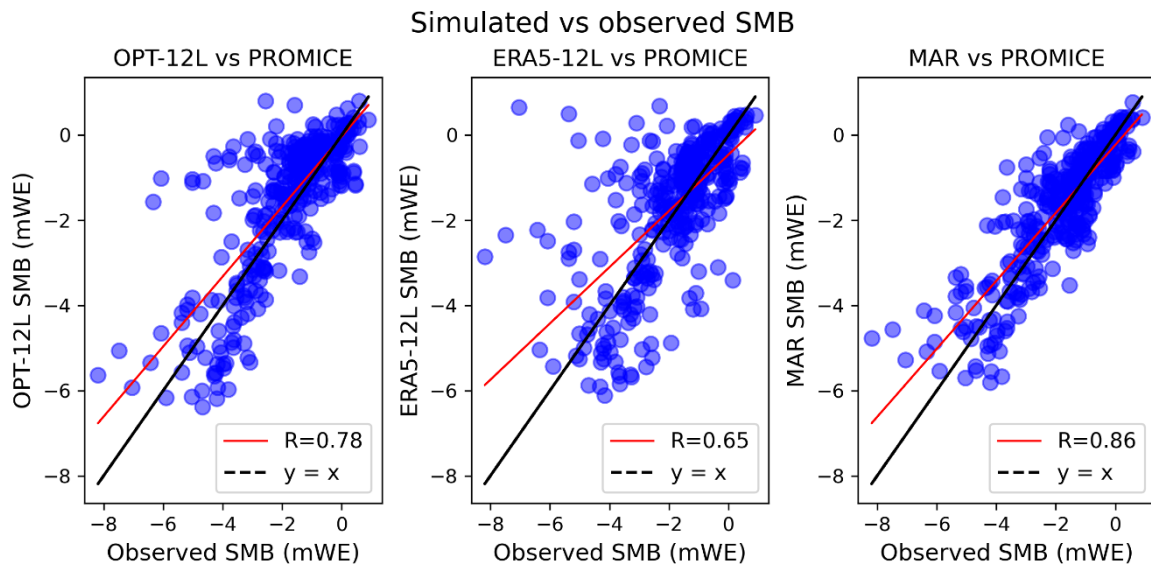
795   **Figure 12:** Simulated SMB in the OPT-12L experiment and in MAR as a function of the observed SMB from the

796   PROMICE network. As the observed SMB values are not all available over the same time interval, the

797   measurements are given in meter water equivalent (mWE). 353 observations were available over the 2000-2019

798   period. Each simulated SMB value corresponds to the grid points located closest to the observation sites. The red

799   line is the regression line with R being the correlation coefficient and the dashed black line indicates the line y =

800   x.

801   The ERA5-12L experiment also produces a good agreement with the observations. Despite a lower correlation

802   coefficient than for MAR and OPT-12L, the mean bias is of the same order of magnitude as that of MAR and the

803   RMSE on the SMB obtained is the lowest for any of the experiments. It is clear that the SMB simulated in the

804   experiments forced by MAR is partly driven by the climate simulated by MAR itself (for the accumulation

805   component). However, the results obtained with ERA5-12L clearly show that the behaviour of our model is

806   consistent whatever the climate forcing used. Nevertheless, it should be reminded that the resolution of

807   ORCHIDEE-ICE corresponds to that of the model used as a forcing. For ERA5-12L, the resolution is about twice

808   as fine as for the experiments forced by MAR (20 km x 20 km). Thus, to make our comparison between ERA5-

809   12L, MAR and/or OPT-12L more robust, we should have used MAR with a resolution of 10 km x 10 km. It cannot

810   therefore be ruled out that the results for OPT-12L would then have provided a better comparison with the

811   PROMICE data than ERA5-12L.

812   **Table 4:** Comparison of the simulated SMB in MAR, STD–3L, STD-12L, ASIM-12L and OPT-12L with the

813   SMB observations from the PROMICE network. The bias is computed as the average between modelled and

814   observed SMB for each grid point. Note that the values of the bias and the RMSE are given in mWE as the observed

815   SMB values are not all available over the same time interval.

Experiments	Bias (mWE)	Correlation	RMSE (mWE)
MAR	0.14	0.86	0.82
STD-3L	0.94	0.67	1.70
STD-12L	0.68	0.73	1.43
ASIM-12L	0.74	0.75	1.33
OPT-12L	0.30	0.78	1.13
ERA5-12L	0.17	0.65	1.07

816   **6. Discussion and concluding remarks**

817   The land surface component of the IPSL ESM used for CMIP6 included a three-layer snowpack model operating

818   over continental surfaces. However, this snow scheme was not adapted to glaciated surfaces, which is a major

819   drawback and makes it impossible to compute the surface mass balance over ice sheets or glaciers. The aim of this

820   paper was therefore to present the new developments made to adapt the snow model to ice-covered areas and to

821   document its performance. Our first step was to calibrate the snow albedo parameterisation over the Greenland ice

822   sheet. To have a set of climate variables covering the whole ice sheet, we chose to force our model by the

823   atmospheric outputs of the MAR regional model which shows very good performances to simulate the surface

824   climate and thus offers undeniable advantages for the representation of the physical processes related to snow and

825   ice, in particular surface melting (Delhasse et al., 2020). We have shown that the ablation-related processes are

826   highly dependent on the choice of the albedo parameters. The set of parameters obtained after manual tuning (OPT-

827   12L experiment) provides a good agreement between the SMB computed in ORCHIDEE-ICE and MAR.

828   However, as outlined in Section 5.2.3, this improvement is mainly the result of albedo lowering. The summer

829   albedo computed with this set of parameters has been degraded compared to MAR and MODIS and to the albedo

830   computed in the ASIM-12L experiment (based on the MODIS-optimised albedo parameters) as shown in Table 3

831   and in Figures 6i-6j and S5, S8. While the RMSEs computed between ORCHIDEE-ICE and MAR for SMB and

832   runoff have been reduced by ~39% and ~33% respectively from ASIM-12L to OPT-12L, the RMSE for albedo

833   has increased by 47% (Table 3). The mismatch between MODIS retrievals and OPT-12L albedo is mainly observed

834   in the northernmost part of the ice sheet and, to a lesser extent, on the western edge.

835 A more objective method would have been to perform a data assimilation experiment similar to the one presented

836 in Raoult et al. (2023) using the new version of the ORCHIDEE-ICE model. However, albedo is not the only

837 important parameter governing the snowpack evolution. The albedo parameters inferred from Raoult et al. (2023)'s

838 optimisation greatly improve the representation of the albedo, but degrade the other model outputs compared to

839 those obtained with the manually-tuned albedo parameters. This is most likely because their optimisation overfits

840 the albedo retrievals without applying constraints to the other processes strongly impacting the SMB components

841 and controlling the state of the snowpack (e.g. snow compaction, snow density, snow viscosity). This supports the

842 recommendation for a multi-objective optimisation using not only albedo data, but also vertical temperature and

843 density profiles as well as SMB observations. Since this type of approach is highly time-consuming, it has not yet

844 been undertaken but could be the objective of a future study.

845 However, the reduction in albedo in the current ORCHIDEE-ICE version can compensate for missing processes.

846 For example, snow drift, transmission of solar radiation, or the effect of light absorbing particles on the albedo are

847 ignored. Metamorphism is not explicitly represented although its effect on the albedo and the vertical density

848 profile are accounted for (albeit in a crude manner) through the snow ageing function f_{age} (Eq. 7) and the ψ_{snow}

849 function (Eq. 17) respectively.

850 In the GrIS, snow erosion has often been considered as a second-order component of mass loss in ablation areas

851 compared to melt water. However, in the ice sheet interior, sublimation and snow erosion are dominant processes

852 in removing mass from the surface, and may have, therefore, a significant impact on SMB (van Angelen et al.,

853 2011).

854 Taking into account the transmission of solar radiation within the snowpack can lead to a warming of the internal

855 layers, with higher temperatures near the surface and lower temperatures at depth due to the exponential decrease

856 in heat transfer. This results in a temperature gradient that influences the metamorphism of snow grains and thus

857 accelerates densification (Colbeck, 1983). We showed that the ORCHIDEE-ICE temperatures inside the snowpack

858 were higher than those simulated by the MAR model. A likely hypothesis to explain this behaviour relies on the

859 reduction in albedo, which leads to excessively high surface temperatures. However, it is important to note that

860 heat transfer can promote snow melting, which in turn can percolate at depth and refreeze, affecting both the runoff

861 and the vertical structure of the snowpack through changes in density (Colbeck, 1983). Quantifying all these

862 processes requires, therefore, the proper representation of solar absorption, which is itself strongly dependent on

863 snow optical properties (Warren, 1982) and, therefore, on snow grain size (Libois et al., 2013). Since

864 metamorphism is not explicitly represented in the model, we assumed that representing solar absorption was not a

865 priority in our modeling approach, even if this choice is debatable. However, in the near future, a more

866 sophisticated albedo scheme based on a transfer radiative model accounting for light-absorbing particles and snow

867 grain size (Kokhannovsky and Zege, 2004) will be implemented in the ORCHIDEE-ICE model. This will allow

868 to represent the backward and forward scattering processes as well as light absorption.

869 In addition, there are also structural deficiencies related to the fact that in ORCHIDEE-ICE, a single energy balance

870 is computed in one grid cell. This is detrimental for the albedo computation especially at the edges of the ice sheet

871 where several surface types may coexist in a 20 km x 20 km mesh. However, the implementation of a multi-tile

872 energy balance is currently under development.

873 Finally, as our simulations have been run in off-line mode, the snow feedback onto the atmosphere has not been

874 taken into account, contrary to the MAR model fully coupled to a snow scheme derived from CROCUS (Brun,

875   1989, 1992). Ignoring snow-atmosphere feedback may potentially lead to biases related to surface processes and

876   to an improper representation of the energy and humidity flux exchanges at the snow-atmosphere interface. For

877   example, forcing our model with the atmospheric temperature at 2m derived from the full coupled MAR simulation

878   could lead to an underestimation of the energy available at the snow-atmosphere interface, resulting in less

879   snowmelt compared to what is simulated in coupled mode. However, our manual tuning approach aims at limiting

880   the potential underestimation of the surface meltwater production. Conversely, any potential bias in the MAR

881   forcing may also affect our results (Dietrich et al., 2024). To overcome this problem, it would have been interesting

882   to force ORCHIDEE-ICE by meteorological fields recorded at the automatic weather stations. This has not been

883   done in this study because the meteorological fields required to force ORCHIDEE-ICE were not all available at

884   the PROMICE stations and because our first objective was to obtain a reasonable estimate of the SMB and its

885   components at the scale of the entire GrIS.

886   Despite the potential improvements that could still be made to ORCHIDEE-ICE to enhance the model's

887   performance, the developments presented in this paper represent a major step forward. Indeed, they now allow the

888   ice-sheet surfaces to be handled by the land surface model, consistently with all the other surface types, and not

889   by the atmospheric component of the IPSL model (LMDZ), as was the case up to now. In addition, the new snow

890   model can now be applied to the continental glaciers replacing the very crude snow scheme used previously. Our

891   developments enable us to provide a reasonable estimate of the surface mass balance of the Greenland ice sheet,

892   in very good agreement with that simulated by the MAR model which was used as a reference in this study. These

893   developments constitute a first step towards the full coupling between the IPSL global climate model and ice-sheet

894   models.

895

896 **Appendix A:**

897 **Table A1:** List of variables used in ORCHIDEE-ICE and related to snowpack and ice processes

Symbol	Variable	Units	Value/Range
α	Surface albedo of the grid cell		
α_{snow}	Albedo of a snow-covered surface		
$\alpha_{snow-free}$	Albedo of snow-free surface		
α_{ice}	Ice albedo		
δ_c	Snowfall thickness necessary for resetting the snow age to zero	kg m^{-2} s^{-1}	
η_{snow}	Snow viscosity	Pa s	
η_0	Snow viscosity parameter	Pa s	3.7 x 10^7
Λ_{snow} (Λ_{ice})	Snow (ice) thermal conductivity	W m^{-1} K^{-1}	
$\Lambda_{eff} = \Lambda_{snow}$	Effective snow thermal conductivity	W m^{-1} K^{-1}	
Λ_{cond}	Snow thermal conductivity	W m^{-1} K^{-1}	
Λ_{vap}	Snow thermal conductivity	W m^{-1} K^{-1}	
λ_{snow}	Integration coefficient for snow thermal profile numerical scheme		
λ_{ice}	Integration coefficient for ice thermal profile numerical scheme		
ρ_{snow}	Snow density	kg m^{-3}	917
ρ_{ice}	Ice density	kg m^{-3}	
ρ_{water}	Water density	Kg m^{-3}	1000
ρ_{air}	Air density	kg m^{-3}	
ρ_t	Parameter of the maximum water holding capacity	kg m^{-3}	200
ρ_ψ	Parameter for the effect of metamorphism in the snow density	kg m^{-3}	150
σ_{snow}^i	Pressure of the snow load over the ith layer	Pa	
τ_{snow}	Snow age	days	
τ_{dec}	Time constant of the albedo decay	days	
τ_{max}	Maximum snow age	days	
ω_1, ω_2	Tuning constants for snow albedo		
A_{aged}	Snow albedo of old snow		

A_i	Surface area of the ith grid point	m^2	
a_η	Snow viscosity parameter	K^{-1}	8.1 x 10^{-2}
a_ψ	Parameter for the effect of metamorphism	s^{-1}	2.8 x 10^{-6}
a_λ	Parameter for snow thermal conductivity	W m^{-1} K^{-1}	0.02
$a_{\lambda v}$	Parameter of snow thermal conductivity from vapor transport	W m^{-1}K^{-1}	-0.06023
a_{ci}	Parameter of heat capacity of the ice	J K^{-1} kg^{-1}	2115.3
$a_{\lambda i}$	Parameter of ice thermal conductivity	W m^{-1} K^{-1}	6.627
B_{dec}	Decay rate of snow albedo		
b_η	Snow viscosity parameter	m^3 kg^{-1}	1.8 x 10^{-2}
b_ψ	Parameter for the effect of metamorphism	K^{-1}	4.2 x 10^{-2}
b_λ	Parameter of snow thermal conductivity	W m^5 K^{-1} kg^{-2}	2.5 10^{-6}
$b_{\lambda v}$	Parameter of snow thermal conductivity from vapor transport	W m^{-1}	-2.5425
b_{ci}	Parameter of heat capacity of the ice	J K^{-2} kg^{-1}	7.79293
$b_{\lambda i}$	Parameter of ice thermal conductivity	K^{-1}	-0.041
c_ψ	Parameter for the effect of metamorphism	m^{3}kg^{-1}	460 m^{3}kg^{-1}
$c_{\lambda v}$	Parameter of snow thermal conductivity from vapor transport	K	-289.99
C_{soil}	Surface heat capacity of soil	J m^{-2} K^{-1}	
C_{snow}	Snow heat capacity	J m^{-2} K^{-1}	
$C_{snow}^v, (C_{ice})$	Snow (ice) volumetric heat capacity	J m^{-3} K^{-1}	
C_{gr_snow}, D_{gr_snow}	Integration coefficients for snow thermal profile numerical scheme		
C_{gr_ice}, D_{gr_ice}	Integration coefficients for ice thermal profile numerical scheme		
D_{snow}^i	Depth of the ith snow layer	m	
D_{lwe}^i	Snow water equivalent in the ith snow layer	m	
D_{ice}^i	Depth of the ith ice layer	m	
dt	ORCHIDEE time step	s	1800
E_{snow}^i (E_{ice}^i)	Energy available to induce phase changes in the snowpack (in the ice)	W m^{-2} s^{-1}	
F_C	Heat conductive flux	W m^{-2}	

f_{age}	Snow age function		
G_{snow}	Surface energy flux over snow-covered areas	W m^{-2}	
G_{surf}	Surface energy flux	W m^{-2}	
H	Sensible heat flux	W m^{-2}	
H_{snow}^{i}	Heat content in the ith snow layer	W m^{-2} s^{-1}	
$H_{rainfall}$	Heat release from rainfall	W m^{-2}	
LE	Latent heat flux	W m^{-2}	
L_s	Latent heat of sublimation	J kg^{-1}	2.8345 10^6
L_f	Latent heat of fusion	J kg^{-1}	333.7
LW_{net}	Net longwave radiation	W m^{-2}	
M_{snow} (M_{ice})	Total amount of snow (ice) melt at each time step	kg m^{-2}s^{-1}	
N	Number of unmasked grid points over the entire Greenland ice-covered area		
N_t	Number of daily time steps over the years 2000-2019		
P	Atmospheric pressure	hPa	
P_0	Reference pressure	hPa	1000
P_{snow}	Snowfall amount during the time step dt	kg m^{-2}s^{-1}	
P_{rain}	Rainfall amount during the time step dt	kg m^{-2}s^{-1}	
Q_{air}	Air specific humidity at 2 m	-	
Q_{sat}	Saturated specific humidity at 2 m	-	
q_{cdrag}	Transfer coefficient	-	
r_{min}	Parameter of the maximum water holding capacity		0.03
r_{max}	Parameter of the maximum water holding capacity		0.10
SCF	Snow cover fraction	-	
S_{snow}	Snow sublimation	kg m^{-2} s^{-1}	
SMB	Surface mass balance	kg m^{-2}s^{-1}	
SW_{net}	Net shortwave radiation	W m^{-2}	
T_{air}	Surface air temperature at 2 m	K	
T_{soil}	Surface temperature	K	

T_0	Freezing temperature	K	273.15
T_{snow}^{add}	Snow temperature adjustment	K	
$T_{snow}\ (T_{ice})$	Snow (ice) temperature	K	
U	Wind speed at 10 m	m s^{-1}	
W_{liq}^{i}	Liquid content in the ith snow layer	m	
W_{max}^{i}	Maximum water holding capacity of the ith snow layer	m	

898

Code availability: The source code for the ORCHIDEE-ICE version used in this study is freely available online via the following address https://doi.org/10.14768/d82899b4-09b4-4337-abb1-75886602fe72 (IPSL Data Catalogue, 2024). The ORCHIDEE model code is written in Fortran 90 and is maintained and developed under a subversion (SVN) control system at the Institut Pierre Simon Laplace (IPSL) in France.

Data availability: The MAR outputs are available at ftp://ftp.climato.be/fettweis (last access 30 October 2020). The MODIS Greenland albedo retrievals MOD10A1 are available at https://doi.org/10.22008/FK2/6JAQPK (last access 22 January 2024, Box et al., 2022). The surface mass balance observations from the PROMICE network are available at https://dataverse.geus.dk/dataverse/PROMICE (last access 06/10/2024, Machguth et al., 2016; Mankoff et al., 2021).

Author contributions: SC conceived the project funding the study. SC, CD, FM and CO co-designed the research and contributed to the code developments. SC and CD performed the preliminary tests with strong support from FM and CO. CD implemented the new snow-layering scheme and the new icy soil type. XF ran the MARv3.11.4 simulations, provided the MAR outputs and performed the comparison between the simulated SMB and the PROMICE dataset. NR provided the albedo parameters obtained from the data assimilation experiment. SC, CD, FM and CO analysed the results with contributions from NR and XF. SC wrote the original draft, with contributions from CD, FM and CO, and generated the figures. SC and PC analysed the vertical temperature and density profiles. All co-authors provided comments on the manuscript.

Competing interests: The authors declare that one of the co-authors is a member of the editorial board of *The Cryosphere*.

Acknowledgements: This study has received funding from Agence Nationale de la Recherche - France 2030 as part of the PEPR TRACCS programme under grant numbers ANR-22-EXTR-0010 and ANR-22-EXTR-0008. The work has also been supported by the French INSU/LEFE OSCAR project. The authors would like to thank all members of the SNOW working group gathering members from the Institut Pierre Simon Laplace (IPSL, France) and the Institut des Géosciences de l'Environnement (IGE, France) for numerous and fruitful discussions. They also thank J.-Y. Peterschmitt for technical support and the core ORCHIDEE team for maintaining the model and especially J. Ghattas for helping merge the ORCHIDEE-ICE code into the trunk version of the model. Data from the Programme for Monitoring of the Greenland Ice Sheet (PROMICE) are provided by the Geological Survey of Denmark and Greenland (GEUS) at http://www.promice.dk. They include sites financially supported by the Glaciobasis programme as part of Greenland Ecosystem Monitoring (https://g-e-m.dk/), maintained by GEUS (ZAK, LYN) and by Asiaq Greenland Survey (NUK_K). The WEG stations are paid for and maintained by the University of Graz.

930

931

References

Alexander, P. M., Tedesco, M., Fettweis, X., van de Wal, R. S. W., Smeets, C. J. P. P., and van den Broeke, M. R.: Assessing spatio-temporal variability and trends in modelled and measured Greenland Ice Sheet albedo (2000–2013), The Cryosphere, 8, 2293–2312, doi: org/10.5194/tc-8-2293-2014, 2014.

Armstrong, R. L. and Brun, E.: Snow and Climate: Physical processes, surface energy exchange and modeling, Cambridge University Press, 222p., 2008.

Anderson, E. A.: A point energy and mass balance model of a snow cover, Technical Report NWS 19, National Oceanic and Atmospheric Administration (NOAA), Silver Spring, MD, USA, 150pp., 1976.

Anderson, T. W: On the distribution of the two-sample Cramer von Mises criterion, The Annals of Mathematical Statistics, 33, 1148–1159, 1962.

Bakker, P, Schmittner, A., Lenaerts, J. T. M., Abe-Ouchi, A., Bi, D., van den Broecke, M. R., Chan, W. L., Hu, A., Beadling, R. L., Marsland, S. J., Mernild, S. H., Saenko, O. A., Swingedouw, D., Sullivan, A. and Yin, J.: Fate of the Atlantic Meridional Overturning Circulation: Strong decline under continued warming and Greenland melting, Geophysical Research Letters, 43, 12,252–12,260, doi:10.1002/2016GL070457, 2016.

Bennartz, R., Shupe, M. D., Turner, D.D., Walden, V. P., Steffen, K., Cox, C. J., Kulie, M. S., Miller, N. B. and Pettersen, C.: July 2012 Greenland melt extent enhanced by low-level liquid clouds, Nature 496, 83-86, doi: 10.1038/nature120002, 2013.

Bonelli, S., Charbit, S., Kageyama, M., Woillez, M.-N., Ramstein, G., Dumas, C. and Quiquet A.: Investigating the evolution of major Northern Hemisphere ice sheets during the last glacial cycle, Climate of the Past, 5, 329-245, doi: 10.5194/cp-5-329-2009, 2009.

Boone, A., and Etchevers, P.: An intercomparison of three snow schemes of varying complexity coupled to the same land surface model: Local-scale evaluation at an Alpine site. Journal of Hydrometeorology, 2(4), 374-394, 2001.

Boucher, O., Servonnat, J., Albright, A. L., Aumont, O., Balkanski, Y., Bastrikov, V., et al.: Presentation and evaluation of the IPSL-CM6A-LR climate model, Journal of Advances in Modeling Earth Systems, 12, e2019MS002010, doi: 10.1029/2019MS002010, 2020.

Bougamont, M., Bamber, J. L., Ridley, J. K., Gladstone, R. M., Greuell, W., Hanna, E., Payne, A. J and Rutt, I.: Impact of model physics on estimating the surface mass balance of the Greenland ice sheet, Geophysical Research Letters, 34, L17501, doi:10.1029/2007GL030700, 2007.

Born, A., Imhof, M. A., and Stocker, T. F.: An efficient surface energy-mass balance model for snow and ice, The Cryosphere, 13, 1529-1546, doi: 10.5194/tc-13-1529-2019, 2019.

Box, J. E., Fettweis, X., Stroeve, J. C., Tedesco, M., Hall, D. K., and Steffen, K.: Greenland ice sheet albedo feedback: thermodynamics and atmospheric feedbacks, The Cryosphere, 6, 821-839, doi: 10.5194/tc-821-2012, 2012.

Box, J. E., van As, D., and Steffen, K.: Greenland, Canadian and Icelandic land-ice albedo grids (2000–2016), GEUS Bulletin, 38, 53–56, doi: 10.34194/geusb.v38.4414, 2017.

Brun, E., Martin, E., Simon, V., Gendre, C. and Coleou, C.: An energy and mass model of snow cover suitable for operational avalanche forecasting, Journal of Glaciology, 35 (121), 333-342, doi: 10.3189/S0022143000009254, 1989.

Brun, E., David, P., Sudul, M., and Brunot, G.: A numerical model to simulate snow cover stratigraphy for operational avalanche forecasting, Journal of Glaciology, 38 (128), 13–22, doi: 10.3189/S0022143000009552, 1992.

Chalita, S. and Le Treut, H.: The albedo of temperate and boreal forest and the Northern Hemisphere climate: a sensitivity experiment using the LMD GCM, Climate Dynamics, 10, 231-240, doi: 10.1007/BF00208990, 1994.

977 Charbit, S., Kageyama, M., Roche, D., Ritz, C; and Ramstein, G.: Investigating the mechanisms leading to the
978   deglaciation of past continental Northern hemisphere ice sheets with the CLIMBER-GREMLINS coupled
979   model, Global and Planetary changes, 48, 253-273, doi: 10.1016/j.gloplacha.2005.01.002, 2005.

980 Charbit, S., D. Paillard, and G. Ramstein (2008), Amount of CO2 emissions irreversibly leading to the total melting
981   of Greenland, Geophysical Research Letters, 35, L12503, doi:10.1029/2008GL033472, 2008.

982 Charbit, S., Dumas, C., Kageyama, M., Roche, D. M. and Ritz, C.: Influence of ablation-related processes in the
983   build-up of Northern Hemisphere ice sheets during the last glacial cycle, The Cryosphere, 7, 681-698, doi:
984   10.5194/tc-7-681-2013, 2013.

985 Cheruy, F., Ducharne, A., Hourdin, F., Musat, I., Vignon, É., Gastineau, G., et al.: Improved near-surface
986   continental climate in IPSL-CM6A-LR by combined evolutions of atmospheric and land surface physics,
987   Journal of Advances in Modeling Earth Systems, 12, e2019MS002005., doi: 10.1029/2019MS002005, 2020.

988 Colbeck, S. C.: Theory of metamorphism of dry snow, Journal of Geophysical Research, 88(C9), 5475-5482, 1983

989 Cristea, N. C., Bennett, A., Nijssen, B. and Lundquist, J. D.: When and where are multiple snow layers important
990   for simulations of snow accumulation and melt? Water Resources Research, 58, e2020WR028993, doi:
991   10.1029/2020WR028993, 2022.

992 Cullather, R.I., Nowicki, S.M.J., Zhao, B. and Suarez, M.J.: Evaluation of the Surface Representation of the
993   Greenland Ice Sheet in a General Circulation Model, Journal of Climate, 27(13), 4835–4856, doi:10.1175/jcli-
994   d-13-00635.1, 2014.

995 Decharme, B., Brun, E., Boone, A., Delire, C., Le Moigne, P. and Morin., S.: Impacts of snow and organic soils
996   parameterization on northern Eurasian soil temperature profiles simulated by the ISBA land surface model,
997   The Cryosphere, 10, 853_877, doi: 10.5194/tc-10-853-2016, 2016.

998 Dee, D. P., Uppala, S. M., Simmons, A. J., Berrisford, P., Poli, P., Kobayashi, S., Andrae, U., Balmaseda, M.A.,
999   Balsamo, G., Bauer, P., Bechtold, P., Beljaars, A., C., M., van de Berg, L., Bidlot, J., Bormann, N., Delsol, C.,
1000   Dragani, R., Fuentes, M., Geer, A.J., Haimberger, L., Healy, S. B., Hersbach, H., Hólm, E.V., Isaksen, L.,
1001   Kallberg, P., Köhler, M., Matricardi, M., McNally, A.P., Monge-Sanz, B. M., Morcrette, J.-J., Park, B.-K.,
1002   Peubey, C., de Rosnay, P,. Tavolato, C., Thépaut, J.-N. and Vitart, F.: The ERA-Interim reanalysis:
1003   configuration and performance of the data assimilation system. Quaterly Journal of the Royal Meteorological
1004   Society, 137, 553–597, doi:10.1002/qj.828, 2011.

1005 Delhasse, A., Kittel, C., Amory, C., Hofer, S., van As, D., S. Fausto, R., and Fettweis, X.: Brief communication:
1006   Evaluation of the near-surface climate in ERA5 over the Greenland Ice Sheet, The Cryosphere, 14, 957–965,
1007   doi:10.5194/tc-14-957-2020, 2020.

1008 De Ridder, K, and Schayes G: The IAGL land surface model: Journal of Applied Meteorology, 36, 167-182,
1009   doi:10.1086/451461, 1997.

1010 Dietrich, L. J., Steen-Larsen, H. C., Wahl, S., Faber, A.-K., and Fettweis, X.: On the importance of the humidity
1011   flux for the surface mass balance in the accumulation zone of the Greenland Ice Sheet, The Cryosphere, 18,
1012   289–305, doi: 10.5194/tc-18-289-2024, 2024.

1013 Domine, F., Picard, G., Morin, S., Barrere, M., Madore, J.-B., & Langlois, A.: Major issues in simulating some
1014   Arctic snowpack properties using current detailed snow physics models: Consequences for the thermal
1015   regime and water budget of permafrost, Journal of Advances in Modeling Earth Systems, 11, 34–44.
1016   https://doi.org/10.1029/2018MS001445, 2019.

1017 Dutra, E. Balsamo, E., Viterbo, P., Miranda, P. M. A., Beljaars, A., Schär, C. and Elder, K.: An Improved Snow
1018   Scheme for the ECMWF Land Surface Model: Description and Offline Validation, Journal of
1019   Hydrometeorology, 11(4); 899-916, doi: 10.1175/2010JHM1249.1, 2010.

1020 Edwards, T. L., Fettweis, X., Gagliardini, O., Gillet-Chaulet, F., Goelzer, H., Gregory, J. M., Hoffman, M.,
1021   Huybrechts, P., Payne, A.J., Perego, M., Price, S., Quiquet, A. and Ritz, C.: Effect of uncertainty in surface

1022 mass balance–elevation feedback on projections of the future sea level contribution of the Greenland ice sheet,
1023   The Cryosphere, 8, 195-208, doi: 10.5194/tc-8-195-2014, 2014.

1024 Enderlin, E. M., Howat, I. M., Jeong, S. Noh, M.-J., van Angelen, J. H. and van den Broeke, M. R. An improved
1025   mass budget for the Greenland ice sheet, Geophysical Research Letters, 41, 866–872,
1026   doi:10.1002/2013GL059010, 2014.

1027 Eyring, V., Bony, S. Meehl, G. A. Senior, C. A., Stevens, B., Stouffer, R. and Taylor, K. E.: Overview of the
1028   Coupled Model Intercomparison Project Phase 6 (CMIP6) experimental design and organization, Geoscientific
1029   Model Development, 9, 1937-1958, doi: 10.5194/gmd-9-1937-2016, 2016.

1030 Fausto, R. S., van As, D., Mankoff, K. D., Vandecrux, B., Citterio, M., Ahlstrøm, A. P., et al.: Programme for
1031   Monitoring of the Greenland Ice Sheet (PROMICE) automatic weather station data, Earth System Scientific
1032   Data, 13, 3819-3845, doi: 10.5194/essd-13-3819-2021, 2021.

1033 Fettweis, X., Box, J. E., Agosta, C., Amory, C., Kittel, C., Lang, C., van As, D., Machguth, H., and Gallée, H.:
1034   Reconstructions of the 1900–2015 Greenland ice sheet surface mass balance using the regional climate MAR
1035   model, The Cryosphere, 11, 1015–1033, https://doi.org/10.5194/tc-11-1015-2017, 2017.

1036 Fettweis, X. Hofer, S., Krebs-Kanzow, U., Amory, C., Aoki, T., Berends, C. J., et al.: GrSMBMIP:
1037   Intercomparison of the modelled 1980-2012 surface mass balance over the Greenland Ice sheet, The
1038   Cryosphere, 14, 3935-3958, doi: 10.5194/tc-14-3935-2020, 2020.

1039 Flanner, M. G., and C. S. Zender: Linking snowpack microphysics and albedo evolution, Journal of Geophysical
1040   Research., 111, D12208, doi:10.1029/2005JD006834.

1041 Fox-Kemper, B., H.T. Hewitt, C. Xiao, G. Aðalgeirsdóttir, S.S. Drijfhout, T.L. Edwards, N.R. Golledge, M.
1042   Hemer, R.E. Kopp, G. Krinner, A. Mix, D. Notz, S. Nowicki, I.S. Nurhati, L. Ruiz, J.-B. Sallée, A.B.A.
1043   Slangen, and Y. Yu: Ocean, Cryosphere and Sea Level Change. *In Climate Change 2021:* The Physical Science
1044   Basis. Contribution of Working Group I to the Sixth Assessment Report of the Intergovernmental Panel on
1045   Climate Change [Masson-Delmotte, V., P. Zhai, A. Pirani, S.L. Connors, C. Péan, S. Berger, N. Caud, Y. Chen,
1046   L. Goldfarb, M.I. Gomis, M. Huang, K. Leitzell, E. Lonnoy, J.B.R. Matthews, T.K. Maycock, T. Waterfield,
1047   O. Yelekçi, R. Yu, and B. Zhou (eds.)]. Cambridge University Press, Cambridge, United Kingdom and New
1048   York, NY, USA, pp. 1211–1362, doi:10.1017/9781009157896.011, 2021.

1049 Franco, B., Fettweis, X., Lang, C., and Erpicum, M.: Impact of spatial resolution on the modelling of the Greenland
1050   ice sheet surface mass balance between 1990–2010, using the regional climate model MAR, The Cryosphere,
1051   6, 695–711, doi: 10.5194/tc-6-695-2012, 2012.

1052 Fréville, H : Observation et simulation de la température de surface en Antarctique : application à l'estimation de
1053   la densité superficielle de la neige. (PhD), Université Paul Sabatier, Toulouse III, Toulouse. Retrieved from
1054   https://tel.archives-ouvertes.fr/tel-01512722, 2015.

1055 Fyke, J., Sergienko, O., Löfverström, M., Price, S. and Lenaerts, J. T., M.: An overview of interactions and
1056   feedbacks between ice sheets and the Earth system, Review of Geophysics, 56, doi: 10.1029/2018GR000600,
1057   2018.

1058 Gallée, H. and Schayes, G.: Development of a three-dimensional meso-primitive equations model: Katabatic winds
1059   simulation in the area of Terra Nova Bay, Antarctica, Monthly Weather Review, 122, 671–685, doi:
1060   10.1175/1520-0493(1994)122%3C0671:DOATDM%3E2.0.CO;2, 1994.

1061 Hahn, L. C., Storelvmo, T., Hofer, S., Parfitt, R. and Ummenhofer, C. C.: Importance of orography for Greenland
1062   ice sheet cloud and melt response to atmospheric blocking, Journal of Climate, 33, 4187-4206, doi:
1063   10.1175/JCLI-D-19_0527.1, 2020.

1064 Hall, D. and Riggs, G.: MODIS/Terra Snow Cover Daily L3 Global 500m Grid, Version 6. Greenland coverage.,
1065   National Snow and Ice Data Center, NASA Distributed Active Archive Center, Boulder, Colorado USA.,
1066   http://nsidc.org/data/MOD10A1/versions/6, accessed December 2016., 2016.

Hall, D. K., Riggs, G. A., and Salomonson, V. V.: Development of methods for mapping global snow cover using moderate resolution imaging spectroradiometer data, Remote sensing of Environment, 54, 127–140, doi: 10.1016/0034-4257(95)00137-P, 1995, 1995.

He, C., Flanner, M., Lawrence, D. M., and Gu, Y.: New features and enhancements in community land model (CLM5) snow albedo modeling: Description, sensitivity, and evaluation, Journal of Advances in Modeling Earth Systems, 16, e2023MS003861, doi: org/10.1029/2023MS003861, 2024.

Helsen, M. M., van de Wal, R. S. W., Reerink, T. J., Bintanja, R., Madsen, M. S., Yang, S., Li, Q., and Zhang, Q.: On the importance of the albedo parameterization for the mass balance of the Greenland ice sheet in EC-Earth, The Cryosphere, 11, 1949–1965, doi: 10.5194/tc-11-1949-2017, 2017.

Hersbach, H., Bell, B., Berrisford, P., Hirahara, S., Horányi, A., Muñoz-Sabater, J., Nicolas, J., Peubey, C., Radu, R., Schepers, D., Simmons, A., Soci, C., Abdalla, S., Abellan, X., Balsamo, G., Bechtold, P., Biavati, G., Bidlot, J., Bonavita, M., De Chiara, G., Dahlgren, P., Dee, D., Diamantakis, M., Dragani, R., Flemming, J., Forbes, R., Fuentes, M., Geer, A., Haimberger, L., Healy, S., Hogan, R.J., Hólm, E., Janisková, M., Keeley, S., Laloyaux, P., Lopez, P., Lupu, C., Radnoti, G., de Rosnay, P., Rozum, I., Vamborg, F., Villaume, S. and Thépaut, J.-N.: The ERA5 global reanalysis. Quarterly Journal of the Royal Meteorological Society, 146, 1999–2049. doi: 10.1002/qj.3803, 2020.

Hourdin, F., Musat, I., Bony, S., Braconnot, P., Codron, F., Dufresne, J., Fairhead, L., Filiberti, M., Friedlingstein, P., Grandpeix, J., Krinner, G., Le Van, P., Li, Z.-X., and Lott, F.: The LMDZ4 general circulation model: climate performance and sensitivity to parametrised physics with emphasis on tropical convection, Climate Dynamics, 27, 787–813, doi:10.1007/s00382-006-0158-0, 2006.

Kageyama, M., Charbit, S., Ritz, C., Khodri, M. and Ramstein G.: Quantifying ice-sheet feedbacks during the last glacial inception, Geophysical Research Letters, 31, L24203, doi:10.1029/2004GL021339, 2004.

Kojima, K.: Densification of seasonal snow cover. Physics of Snow and Ice: Proceedings of the International Conference on Low Temperature Science, Part 1, Sapporo, Japan, Hokkaido University, 1 (2), 929–952, 1967.

Kokhanovsky, A. A. and Zege, E. P.: Scattering optics of snow, Applied Optics, 43, 1589–1602, 2004.

Krinner, G., Viovy, N., de Noblet-Ducoudré, N., Ogée, J., Polcher, J., Friedlingstein, P., Ciais, P., Sitch, S., and Prentice, I. C.: A dynamic global vegetation model for studies of the coupled atmosphere-biosphere system, Global Biogeochemical Cycles, 19, GB1015, doi:10.1029/2003GB002199, 2005.

Lawrence, D. M., Fisher, R. A., Koven, C. D., Oleson, K. W., Swenson, S. C., Bonan, G., Collier, N., Ghimire, B., van Kampenhout, L., Kennedy, D., Kluzek, E., Lawrence, P. J., Li, F., Li, H., Lombardozzi, D., Riley, W. J., Sacks, W. J., Shi, M., Vertenstein, M., Wieder, W. R., Xu, C., Ali, A. A., Badger, A. M., Bisht, G., van den Broeke, M., Brunke, M. A., Burns, S. P., Buzan, J., Clark, M., Craig, A., Dahlin, K., Drewniak, B., Fisher, J. B., Flanner, M., Fox, A. M., Gentine, P., Hoffman, F., Keppel-Aleks, G., Knox, R., Kumar, S., Lenaerts, J., Leung, L. R., Lipscomb, W. H., Lu, Y., Pandey, A., Pelletier, J. D., Perket, J., Randerson, J. T., Ricciuto, D. M., Sanderson, B. M., Slater, A., Subin, Z. M., Tang, J., Thomas, R. Q., Val Martin, M., and Zeng, X.: The Community Land Model Version 5: Description of New Features, Benchmarking, and Impact of Forcing Uncertainty, Journal of Advances in Modeling Earth Systems., 11, 4245–4287, doi: 10.1029/2018MS001583, 2019.

Lefebre, F., Gallée, H., van Ypersele, J.-P. and W. Greuell, Modeling of snow and ice melt at ETH Camp (West Greenland): A study of surface albedo, Journal of Geophysical Research, 108(D8), 4231, doi:10.1029/2001JD001160, 2003.

Libois, Q., Picard, G., France, J. L., Arnaud, L., Dumont, M., Carmagnola, C. M., and King, M. D.: Influence of grain shape on light penetration in snow, The Cryosphere, 7, 1803–1818, https://doi.org/10.5194/tc-7-1803-2013, 2013.

Louis, J. F.: A parametric model of vertical eddy fluxes in the atmosphere. *Boundary-Layer Meteorology*, *17*(2), 187-202, 1979.

Lynch-Stieglitz, M.: The development and validation of a simple snow model for the GISS GCM, Journal of Climate, 7, 1842-1855, doi: 10.1175/1520-0442(1994)007%3C1842:TDAVOA%3E2.0.CO;21994, 1994.

Martin, T., Biastoch, A., Lohmann, G., Mikolajewicz, U., and Wang, X.: On timescales and reversibility of the ocean's response to enhanced Greenland Ice Sheet melting in comprehensive climate models. Geophysical Research Letters, 49, e2021GL097114. doi: 10.1029/2021GL097114, 2022.

Machguth, H., Thomsen, H. H., Weidick, A., Abermann, J., Ahlström, A. P., Andersen, M. L., Andersen, S. B., Björk, A. A., Box, J. E., Braithwaite, R. J., Bøggild, C. E., Citterio, M., Clement, P., Colgan, W., Fausto, R. S., Gleie, K., Hasholt, B., Hynek, B., Knudsen, N. T., Larsen, S. H., Mernild, S., Oerlemans, J., Oerter, H., Olesen, O. B., Smeets, C. J. P. P., Steffen, K., Stober, M., Sugiyama, S., van As, D., van den Broeke, M. R., and van de Wal, R. S.: Greenland surface mass balance observations from the ice sheet ablation area and local glaciers, Journal of Glaciology, 62, 861–887, https://doi.org/10.1017/jog.2016.75, 2016.

Maeno N.: The electrical behaviours of Antarctic ice drilled at Mizuho Station, East Antarctica Memoirs of the National Institute of Polar Research 10, 77-94, 1978.

Maeno, N., and Ebinuma, T.: Pressure sintering of ice and its implication to the densification of snow at polar glaciers and ice sheets, Journal of Physical Chemistry, 87, 4103-4110, 1983.

Mankoff, K. D., Fettweis, X., Langen, P. L., Stendel, M., Kjeldsen, K. K., Karlsson, N. B., Noël, B., van den Broeke, M. R., Solgaard, A., Colgan, W., Box, J. E., Simonsen, S. B., King, M. D., Ahlstrøm, A. P., Andersen, S. B., and Fausto, R. S.: Greenland ice sheet mass balance from 1840 through next week, Earth Syst. Sci. Data, 13, 5001–5025, https://doi.org/10.5194/essd-13-5001-2021, 2021.

Marshall, H.P., Conway, H., Rasmussen, L.A.: Snow densification during rain, Cold Regions Science and Technology, 30, 35-41, doi: 10.1016/S0165-232X(99)00011-7, 1999.

Mellor, M.: Snow and Ice on the Earth's Surface, *Cold regions science and engineering. Part 2, Physical science. Sect. C, The physics and mechanics of ice Snow and Ice on the Earth's Surface*, U.S. Army Materiel Command, Cold Regions Research and Engineering Laboratory, 163pp., 1964.

Mizukami, N., and Perica, S.: Spatiotemporal characteristics of snowpack density in the mountainous regions of the western United States. Journal of Hydrometeorology, 9(6), 1416–1426. https://doi.org/10.1175/2008JHM981.1, 2008.

Monin, A. S., and Obukhov, A. M.: Basic laws of turbulent mixing in the surface layer of the atmosphere. *Contrib. Geophys. Inst. Acad. Sci. USSR*, *151*(163), e187, 1954.

Montgomery L, Koenig L, Lenaerts JTM, Kuipers Munneke P (2020). Accumulation rates (2009–2017) in Southeast Greenland derived from airborne snow radar and comparison with regional climate models. Annals of Glaciology 61(81), 225–233, doi: 10.1017/aog.2020.8, 2020.

Muntjewerf, L., Sellevod, R., Vizcaino, M., Ernani da Silva, C., Petrini, M., Thayer-Calder, K., Scherrenberg, M. D. W., Bradley; S. L., Katsman, C. A., Fyke, J., Lipscomb, W. H., Löfverström, M. and Sacks, W.J.: Accelerated Greenland ice sheet mass loss under high greenhouse gas forcing as simulated by the coupled CESM2.1-CISM2.1, Journal of Advances Modeling in Earth Systems, 12, e2019MS002031, doi: 10.1029/2019MS002031, 2020.

Niu, G.-Y., and Yang, Z.-L.: An observation-based formulation of snow cover fraction and its evaluation over large North American river basins, Journal of Geophysical Research, 112, D21101, doi:10.1029/2007JD008674, 2007.

Noël, B., van de Berg, W. J., Machguth, H., Lhermitte, S., Howat, I., Fettweis, X., and van den Broeke, M. R.: A daily, 1 km resolution data set of downscaled Greenland ice sheet surface mass balance (1958–2015), The Cryosphere, 10, 2361–2377, https://doi.org/10.5194/tc-10-2361-2016, 2016.

Noël, B., van de Berg, W. J., van Wessem, J. M., van Meijgaard, E., van As, D., Lenaerts, J. T. M. Lhermitte, S., Kuipers Munneke, P., Smeets, C. J. P. P., van Ulft, L.H., van de Wal, R. S. W., and van den Broeke, M. R.:

Modelling the climate and surface mass balance of polar ice sheets using RACMO2 – Part 1: Greenland (1958–2016), The Cryosphere, 12, 811–831, https://doi.org/10.5194/tc-12-811-2018, 2018.

Pahaut, E.: La métamorphose des cristaux de neige (Snow crystal metamorphosis), Monographies de la Météorologie Nationale, No. 96, Météo France, Direction de la météorologie nationale, France, 58pp., 1976.

Patterson, W. S. B., The Physics of Glaciers, Butterworth-Heinemann, 1994.

Punge, H. J., Gallée, H., Kageyama, M. and Krinner, G.: Modelling snow accumulation on Greenland in Eemian, glacial inception, and modern climates in a GCM, Climate of the Past, 8, 1801–1819, doi: 10.5194/cp-8-1801-2012, 2012, 2012.

Raoult, N., Charbit, S., Dumas, C., Maignan, F., Ottlé, C., and Bastrikov, V.: Improving modelled albedo over the Greenland ice sheet through parameter optimisation and MODIS snow albedo retrievals, The Cryosphere, 17, 2705–2724, https://doi.org/10.5194/tc-17-2705-2023, 2023.

Reeh, N.: Parameterization of melt rate and surface temperature on the Greenland ice sheet, Polarforschung, 5913, 113-128, 1991.

Reynolds, C. A., Jackson, T. J., and Rawls, W. J.: Estimating soil water-holding capacities by linking the Food and Agriculture Organization soil map of the world with global pedon databases and continuous pedotransfer functions, Water Resources Research, 36, 3653–3662, doi: 10.1029/2000WR900130, 2000.

Ridley, J. K., Huybrechts, P., Gregory, J. M. and Lowe, J. A.: Elimination of the Greenland ice sheet in a high CO_2 climate, Journal of Climate, 18, 3409-3427, doi: 10.1175/JCLI3482.1, 2005.

Riihelä, A., King, M. D. and Anttila K.: The surface albedo of the Greenland ice sheet between 1982 and 2015 from CLARA-A2 dataset and its relationship to the ice sheet's surface mass balance, The Cryosphere, 13, 2597-2614, doi: 10.5194/tc-13-2597-2019, 2019.

Roche, D. M., Dumas, C., Bügelmayer, M., Charbit, S. and Ritz, C.: Adding a dynamical cryosphere to iLOVECLIM (version 1.0): coupling with the GRISLI ice-sheet model, Geoscientific Model Development, 7, 1377-1394, doi: 10.5194/gmd-7-1377-2014, 2014.

Ryan, J.V., Smith, L. C., van As, D., Cooley, S. W., Cooper, M. G., Pitcher, L. H., and Hubbard, A.: Greenland Ice Sheet surface melt amplified by snowline migration and bare ice exposure, Science Advances, 5, eaav3738, doi: 10.1126/sciadv.aav3738, 2019.

Sellevod, R., van Kampenhout, L., Lenaerts, J. T. M., Noël, B., Lipscomb, W. H. and Vizcaino, M.: Surface mass balance downscaling through elevation classes in an Earth system model: application to the Greenland ice sheet, The Cryosphere, 13, 3193-3208, doi: 10.5194/tc-13-3193-2019, 2019.

Smith, R. S., Mathiot P., Siahaan, A., Lee, V., Cornford, S. L., Gregory, J. M., Payne, A. J., Jenkins, A., Holland, P., R., Ridley, J. K. and Jones, C. G.: Coupling the U.K. Earth System Model to dynamic models of the Greenland and Antarctic ice sheets, Journal of Advances Modeling in Earth Systems, 13, e2021MS002520, doi: 10.1029/2021MS002520, 2021.

Smith, B. E., Medley, B., Fettweis, X., Sutterley, T., Alexander, P., Porter, D., and Tedesco, M.: Evaluating Greenland surface-mass-balance and firn-densification data using ICESat-2 altimetry, The Cryosphere, 17, 789–808, doi: 10.5194/tc-17-789-2023, 2023.

Stephens, M. A.: Use of the Kolmogorov-Smirnov, Cramer-von Mises and related statistics without extensive tables, Journal of the Royal Statistical Society Series B (Methodological), 32 (1), 115-122, 1970.

Sun, S., Jin, J. and Xue, Y.: A simple snow-atmosphere-soil transfer model, Journal of Geophysical Research, 104 (D16), 19587-19597, doi: 10.1029/1999JD900305, 1999.

Taylor, K. E., Stouffer, R. J. and Meehl, G. A.: An overview of CMIP5 and the experiment design, Bulletin of American Meteorological Society, 93, 485-498, doi: 10.1175/BAMS-D-11-00094.1, 2012.

Tedesco, M. and Fettweis, X.: Unprecedented atmospheric conditions (1948–2019) drive the 2019 exceptional melting season over the Greenland ice sheet, The Cryosphere, 14, 1209–1223, https://doi.org/10.5194/tc-14-1209-2020, 2020.

The IMBIE team: Mass balance of the Greenland ice sheet from 1992 to 2018, Nature, 579, 233-239, doi: 10.1038/s41586-019-1855-2, 2020.

Uppala, S.M., Kållberg, P.W., Simmons, A.J., Andrae, U., da Costa Bechtold, V., Fiorino, M., Gibson, J.K., Haseler, J., Hernandez, A., Kelly, G.A., Li, X., Onogi, K., Saarinen, S., Sokka, N., Allan, R.P., Andersson, E., Arpe, K., Balmaseda, M.A., Beljaars, A.C.M., van de Berg, L., Bidlot, J., Bormann, N., Caires, S., Chevallier, F., Dethof, A., Dragosavac, M., Fisher, M., Fuentes, M., Hagemann, S., Hólm, E.V., Hoskins, B.J., Isaksen, L., Janssen, P.A.E.M., Jenne, R., McNally, A.P., Mahfouf, J.-F., Morcrette, J.-J., Rayner, N.A., Saunders, R.W., Simon, P., Sterl, A., Trenberth, K.E., Untch, A., Vasiljevic, D., Viterbo, P. and Woollen, J.: The ERA-40 re-analysis. *Quarterly Journal of the Royal Meteorological Society*, 131, 2961–3012, 2005.

Urraca, R., Lanconelli, C., Cappucci, F., Gobron, N.: Comparison of Long-Term Albedo Products against Spatially Representative Stations over Snow, Remote Sensing 14, 3745, doi: 10.3390/rs14153745, 2022.

Urraca, R., Lanconelli, C., Cappucci, F., Gobron, N. : Assessing the fitness of satellite albedo products for monitoring snow albedo trends, IEEE Transactions on geoscience and remote sensing, 61, 4404817, doi: 10.1109/TGRS2023.3281188, 2023.

van Angelen, J. H., van den Broeke, M. R., and van de Berg, W. J.: Momentum budget of the atmospheric boundary layer over the Greenland ice sheet and its surrounding seas, Journal of Geophysical Research-Atmophere., 116, D10101, doi:10.1029/2010JD015485, 2011.

van den Broeke, M., Bamber, J., Ettema, J., Rignot, E., Schrama, E., van de Berg, W. J., van Meijgaard, E., Velicogna, I., Wouters, B.: Partitioning recent Greenland mass loss, Science, 326, 984-986, doi: 10.1126/science1178276, 2009.

van den Broeke, M., Enderlin, E. M., Howat, I. M., Kuipers Munnneke, P., Noël, B. P. Y., van de Berg, W. J., van Meijgaard, E., Wouters, B.: On the recent contribution of the Greenland ice sheet to sea level change, The Cryosphere, 10, 1933-1946, doi: 10.5194/tc-10-1933-2016, 2016.

van de Wal, R., S., W.: Mass-balance modelling of the Greenland ice sheet: a comparison of an energy-balance and a degree-day model, Annals of Glaciology, 23, 36-45, 1996.

Vionnet, V. Brun, E., Morin, S., Boone, A., Faroux, S., Le Moigne, P., Martin, E. and Willemet J.-M.: The detailed snowpack scheme Crocus and its implementation in SURFEX v7.2, Geoscientific Model Development, 5, 773-791, doi: 10.5194/gmd-5-773-2012, 2012.

Vizcaino, M., Mikolajewicz, U., Jungclaus, J. and Schurgers, G.: Clmate modification by future ice sheet changes and consequences for ice sheet mass balance, Climate Dynamics, 34, 301-324, doi: 10.1007/s00382-009-0591-y, 2010.

Vizcaino, M., Lipscomb, W. H., Sacks, W. J., van Angelen, J. H., Wouters, B. and van den Broeke, M. R.: Greenland surface mass balance as simulated by the Community Earth System Model. Part I: Model evaluation and 1850-2005 results, Journal of Climate, 26, 7793-7812, doi: 10.1175/JCLI-D-00615.1, 2013.

Vizcaino, M.: Ice sheets as interactive components of Earth System Models: progress and challenges, WIREs Climate Change, 5, 557–568. doi: 10.1002/wcc.285, 2014.

Wang, T., Ottlé, C., Boone, A., Ciais, P., Brun, E., Morin, S., Krinner, G., Piao, S. and Peng, S.: Evaluation of an improved intermediate complexity snow scheme in the ORCHIDEE land surface model, Journal of Geophysical Research Atmosphere, 118, 6064–6079, doi:10.1002/jgrd.50395, 2013.

Wang, T., Peng, S., Krinner, G., Ryder, J., Li, Y., Dantec-Nédélec, S. and Ottlé, C.: Impacts of Satellite-Based Snow Albedo Assimilation on Offline and Coupled Land Surface Model Simulations. PLoS ONE 10(9): e0137275, doi:10.1371/journal.pone.0137275, 2015.

1246 Wang, F., Cheruy, F., and Dufresne, J.-L.: The improvement of soil thermodynamics and its effects on land surface
1247 meteorology in the IPSL climate model, Geoscientific Model Development., 9, 363–381,
1248 https://doi.org/10.5194/gmd-9-363-2016, 2016.

1249 Warren S.: Optical properties of snow. Reviews of Geophysics and Space Physics, 20(1), 67-89, 1982.

1250 Yang, Z., Chen, R., Liu, Y., Zhao, Y., Liu, Z., & Liu, J.: The impact of rain-on-snow events on the snowmelt
1251 process: A field study, Hydrological Processes, 37(11), e15019; doi: 10.1002/hyp.15019, 2023.

1252 Yen, Y.-C.: Review of thermal properties of snow, ice and sea ice.Cold Regions Research and Engineering
1253 Laboratory, Hanover, NH, 1981.